Magnesium and calcium silicate hydrates, Part I: Investigation of the possible magnesium incorporation in calcium silicate hydrate (C-S-H) and of the calcium in magnesium silicate hydrate (M-S-H)

Ellina Bernard, Barbara Lothenbach, Céline Cau-Dit-Coumes, Christophe Chlique, Alexandre Dauzeres, Isabelle Pochard

Accepted Manuscript

Magnesium and calcium silicate hydrates, part I: Investigation of the possible magnesium incorporation in calcium silicate hydrate (C-S-H) and of the calcium in magnesium silicate hydrate (M-S-H)

Ellina Bernard, Barbara Lothenbach, Céline Cau-Dit-Coumes, Christophe Chlique, Alexandre Dauzères, Isabelle Pochard

PII: S0883-2927(17)30369-4

DOI: 10.1016/j.apgeochem.2017.12.005

Reference: AG 4000

To appear in: *Applied Geochemistry*

Received Date: 20 July 2017

Revised Date: 4 December 2017

Accepted Date: 5 December 2017

Please cite this article as: Bernard, E., Lothenbach, B., Cau-Dit-Coumes, Cé., Chlique, C., Dauzères, A., Pochard, I., Magnesium and calcium silicate hydrates, part I: Investigation of the possible magnesium incorporation in calcium silicate hydrate (C-S-H) and of the calcium in magnesium silicate hydrate (M-S-H), *Applied Geochemistry* (2018), doi: 10.1016/j.apgeochem.2017.12.005.

Magnesium and calcium silicate hydrates, Part I: Investigation of the possible magnesium incorporation in calcium silicate hydrate (C-S-H) and of the calcium in magnesium silicate hydrate (M-S-H)

Ellina Bernard[1)*], Barbara Lothenbach[1)], Céline Cau-Dit-Coumes[2)], Christophe Chlique[2)], Alexandre Dauzères[3)], Isabelle Pochard[4)]

[1)] Empa, Laboratory for Concrete & Construction Chemistry, 8600 Dübendorf, Switzerland

[2)] CEA, DEN, DE2D, SEAD, F-30207 Bagnols-sur-Cèze cedex, France

[3)] IRSN, Institute of Radiation Protection and Nuclear Safety, PSE/SEDRE/LETIS, BP 17, 92262 Fontenay aux Roses, France

[4)] Université Bourgogne-Franche-Comté, 21078 Dijon, France

*Corresponding author: Bernard E., email: ellina.bernard@empa.ch

Abstract

Calcium silicate hydrate (C-S-H) and magnesium silicate hydrate (M-S-H) have been described as two separate phases. This work investigates their stability domains and the possible uptake of small amounts of magnesium by C-S-H or, reversely, the uptake of small amounts of calcium by M-S-H. The phases, synthesized by co-precipitation, are characterized using a large panel of techniques (thermogravimetry analysis, X-ray diffraction, X-ray pair distribution function analysis, ^{29}Si MAS-NMR spectroscopy, measurement of zeta potential and cation exchange capacity) while the compositions of the solutions at equilibrium are determined by ion chromatography and pH measurements. Syntheses of C-S-H samples in the presence of magnesium ((Ca+Mg)/Si = 0.8 and Mg/Si = 0.05 or 0.10) yield two separate phases: C-S-H and M-S-H. There is no experimental evidence of any uptake of magnesium by C-S-H. On the contrary, when M-S-H samples are synthesized in the presence of calcium ((Ca+Mg)/Si = 0.8 and Ca/Si

= 0.05 or 0.10), the low pH of the suspension (9-10) prevents the formation of C-S-H but favors the precipitation of M-S-H with small amounts of calcium. This latter may be sorbed onto the surface of M-S-H to outbalance its negative charges and/or incorporated into the interlayer, as suggested by small structural changes.

Keywords

Low-pH cement, calcium silicate hydrate (C-S-H), magnesium silicate hydrate (M-S-H), surface properties, thermodynamic modelling

1. Introduction

The formation of magnesium silicates hydrate (M-S-H), has been observed at the interfacial zone of cement-based materials in contact with clays (Dauzères et al., 2016; Garcia Calvo et al., 2010; Jenni et al., 2014; Lerouge et al., 2017; Mäder et al., 2017) and/or as secondary products from the degradation of cementitious materials by groundwater or seawater (Bonen and Cohen, 1992; Jakobsen et al., 2016; Santhanam et al., 2002). The combination of leaching and carbonation induces a pH decrease at the surface of the cement sample, resulting in the decalcification of calcium silicate hydrate (C-S-H) and the formation of amorphous silica which then reacts with magnesium to yield a Mg-enriched phase referred as magnesium silicate hydrate (M-S-H) (Bonen and Cohen, 1992; Dauzères et al., 2016; De Weerdt and Justnes, 2015; Jakobsen et al., 2016; Jenni et al., 2014; Lerouge et al., 2017; Mäder et al., 2017; Santhanam et al., 2002).

M-S-H phases have been synthesized in the laboratory (Brew and Glasser, 2005; d'Espinose de Lacaillerie et al., 1995; Nied et al., 2016; Roosz et al., 2015; Walling et al., 2015); its structure has also been investigated by molecular modelling (Pedone et al., 2017). Both C-S-H and M-S-H phases exhibit a rather high water content, water being both present in the interlayer or sorbed at the surface, and

integrated in the structure (as H_2O and hydroxyl group (Jin and Al-Tabbaa, 2013; L'Hôpital et al., 2016a; Lothenbach et al., 2016; Nied et al., 2016)). C-S-H consists of calcium oxide layers sandwiched on both side by silicate chains with the typical dreierketten structure (Richardson, 2008). At low Ca/Si ratio, the tetrahedral silicate sites in C-S-H are usually bound to two neighbors (= Q^2, leading to almost infinite chains). In contrast, M-S-H has a layered structure (Brew and Glasser, 2005; Nied et al., 2016; Roosz et al., 2015; Walling et al., 2015) similar to clay minerals and the tetrahedral silicate sites are mainly bound to two or three neighbors (Q^2 and Q^3). As for clays, M-S-H is stable at lower pH values than C-S-H, i.e. at pH between 7.5 (Bernard et al., 2017a) and 10.5 (Bernard et al., 2017b; Nied et al., 2016; Zhang et al., 2011) or even up to 11.5 (Bernard et al., 2017a). Given the different structures and stability domains, most studies (Bernard et al., 2017a; Brew and Glasser, 2005; Chiang et al., 2014; Lothenbach et al., 2015) have reported the precipitation of two distinct phases and not of a mixed magnesium calcium silicate hydrate phase.

The structure of synthetic M-S-H has been related to very poorly crystalline tri-octahedral 2:1 (or 1:1) phyllosilicate. It has also been observed that M-S-H has variable basal spacing (Roosz et al., 2015) similar to clay minerals. In addition, TEM observations indicate the possible uptake of aluminum, iron and calcium in its structure (Lerouge et al., 2017).

This paper is the first part of a study on the stability and the uptake of the magnesium and calcium silicate hydrates and focuses on the possible incorporation of magnesium in C-S-H and of calcium in M-S-H.

Replacement of magnesium oxide by calcium oxide in octahedral sheets of magnesium silicate minerals is not reported in the literature. Mixed magnesium calcium minerals exist as dolomite ($CaMg(CO_3)_2$), which has an alternating structural arrangement of calcium and magnesium ions. In this case, calcium or

magnesium oxides are not mixed in octahedral layers, but in alternate octahedral sites of calcium or magnesium as the crystallographic radius of calcium (0.99Å (Conway, 1981)) in the octahedral layer is significantly higher than that of magnesium (0.65Å (Conway, 1981)). The uptake of calcium in magnesium silicate clay as e.g. saponite occurs at the negatively charged surface and in its interlayer to compensate the charge. Similarly, in the amphibole group, the uptake of calcium can occur as charge balancing Ca^{2+} in the *M4 sites* (i.e. in sites with 6 to 8-fold coordination between two T:O:T[1] blocks).

Even if the formation of a magnesium calcium silicate hydrate phase does not seem very likely, the possible uptake of small amounts of magnesium by C-S-H (Bernard et al., 2017a; Lothenbach et al., 2015) may be envisaged. The uptake of alkalis, sulfate, or aluminum in C-S-H has indeed already been observed (Bach et al., 2013; L'Hôpital et al., 2016b; L'Hôpital et al., 2015; Lothenbach and Nonat, 2015; Plusquellec and Nonat, 2016; Renaudin et al., 2009; Richardson, 2008; Richardson et al., 1993; Skibsted et al., 1993). Alkali and sulfate uptakes occur mainly by sorption onto the surface or in the interlayer, while aluminum is taken up both in the interlayer and in the silicate chains. A high calcium concentration and/or a low pH decrease the alkali uptake (L'Hôpital et al., 2016b). The uptake of ions by C-S-H also decreases with the ions concentration in solution. Magnesium is, as calcium, a double charged cation, with a similar ionic radius in its hydrated state (4.3 Å for Mg^{2+}, 4.1 Å for Ca^{2+}) (Conway, 1981). However in the presence of M-S-H and C-S-H at pH 10-11 (Bernard et al., 2017a; Lothenbach et al., 2015), the aqueous magnesium concentrations are much lower (0.0001-0.1 mmol/L) than those of calcium (0.1-1.5 mmol/L). Hence, the uptake of magnesium(II) by C-S-H is expected to be smaller than the uptake of calcium(II).

This paper investigates the possible uptake of calcium by M-S-H and of magnesium by C-S-H. M-S-H is synthesized in batch experiments in the presence of calcium. Similarly, C-S-H is synthesized in the

[1]T= tetrahedral layer; O= octahedral layer

89 presence of magnesium. The surface charge of the particles in suspension is investigated by zeta
90 potential measurements and their cation exchange capacity (CEC) is determined. The composition of the
91 solutions at equilibrium is analysed by pH measurements and ion chromatography. The solid phases are
92 characterized by thermogravimetry analysis (TGA), powder X-ray diffraction (XRD), and ^{29}Si solid-
93 state MAS NMR.

94 ## 2. Materials and methods

95 ### 2.1. Synthesis

96 All the syntheses were performed in a glovebox under nitrogen atmosphere to minimize CO_2
97 contamination. MgO (Merck, pro analysis, containing 0.18 ± 0.02 wt% Na_2O), CaO (obtained by
98 burning calcium carbonate ($CaCO_3$, Merck, pro analysis) for 12 h at 1000 °C) and SiO_2 (SiO_2, Aerosil
99 200, 0.9 wt% HCl) were directly mixed with ultrapure water as detailed in (Lothenbach et al., 2015) to
100 obtain M-S-H or C-S-H with small amounts of calcium or magnesium. The synthesized products are
101 summarized in Table 1. The syntheses were carried out to obtain ~ 5 g of solid and the water-to-solid
102 (W/S) ratio was set to 45.

103 *Table 1: Labelling and initial composition of mixes of the plain M-S-H and C-S-H samples and of the co-precipitated*
104 *samples. Bold co-precipitated samples correspond to the fully analyzed samples while the Co-0.40 and the Co-0.50*
105 *samples are presented in the paper to supplement the analytical data of the aqueous phase.*

Samples	**M-S-H 0.8**	**Co-0.05**	**Co-0.10**	Co-0.40	Co-0.50	**Co-0.70**	**Co-0.75**	**C-S-H 0.8**
Total Mg/Si	0.8	0.75	0.70	0.40	0.30	0.10	0.05	
Total Ca/Si		0.05	0.10	0.40	0.50	0.70	0.75	0.80
Total (Mg+Ca)/Si	0.80	0.80	0.80	0.80	0.80	0.80	0.80	0.80

106

These suspensions were equilibrated at different temperatures (20°C and 50°C) and for different times (from 6 months up to 2 years) to determine the solubility; these long equilibration times and the increased temperature aimed to provide samples at/or very close to equilibrium (Bernard et al., 2017b).

The solid and liquid phases were separated by filtration under pressure (4-5 bars N_2) using nylon filters (0.45 µm).

Following the filtration, the solids were washed with a 50/50 (volume) water-ethanol mix and then with ethanol (94 wt% alcohol) to remove dissolved ions and to prevent the precipitation of salts during drying (L'Hôpital et al., 2015). The samples were freeze-dried with liquid nitrogen (for approximatively 20 min at -195°C) and kept at -40°C under vacuum (pressure of 0.28 mbar) for 7 days. The solid phases were analyzed after further equilibration in N_2-filled desiccators at a relative humidity of ~30% (saturated $CaCl_2$ solution) for a period of 14 days or longer. After drying, the samples were gently ground by hand.

Pure C-S-H (Bernard et al., 2017a) and pure M-S-H (Bernard et al., 2017b) were analyzed for comparison. In addition, powdered reference mixtures labelled Mix-0.05, Mix-0.10, Mix-0.70 and Mix-0.75 were prepared by mechanical mixing in a grinder, pure C-S-H and pure M-S-H (prepared separately) to obtain the same molar ratios as the co-precipitated samples. In those mixes, the formation of any magnesium calcium silicate hydrate phase (M-C-S-H) could be excluded due to the absence of water.

2.2. Analytical techniques

The composition of the liquid phase was analysed by ion chromatography (IC) immediately after filtration. The dissolved concentrations of Mg, Ca, Si, Na, Cl, K, SO_4 in undiluted solutions or in solutions diluted by a factor 10, 100 or 1000 were quantified using a Dionex DP series ICS-3000 ion

chromatography system with a measurement error ≤ 10%. All concentrations were determined as duplicates and the mean value is given in this paper. Na, Cl, K, SO_4 concentrations were also measured as traces were present in the starting materials. The composition of the aqueous phase of M-S-H did not change significantly during the 30 minutes necessary to cool down the solutions from 50°C to ambient temperature (Bernard et al., 2017b). The pH values (±0.1) were measured at ambient temperature (23±2°C) in an aliquot of the unfiltered suspension and the results were corrected to 20 or 50°C as described in (Bernard et al., 2017b).

Thermogravimetric analyses (TGA) were carried out on ground powder (~30 mg) with a Mettler Toledo TGA/SDTA 8513 instrument using a heating rate of 20°C/min from 30 to 980 °C. The amount of $Mg(OH)_2$ (brucite) was quantified from the water weight loss at around 400-420°C using the tangential method (Lothenbach et al., 2016) and calculated according to the equation (1):

$$wt.\%\ brucite_{dry} = \frac{water\ loss\ (brucite)}{100 - water\ loss_{(30-550°C)}} \times \frac{M_{brucite}}{M_{H2O}} \times 100 \qquad (1)$$

where wt. % brucite $_{dry}$ corresponds to the wt.% of brucite for 100g of dry mass, the water loss is expressed in wt. %, the $M_{brucite}$ is taken equal to 58.32 g/mol, while the M_{H2O} is taken equal to 18.02 g/mol. The relative error on the brucite content is ± 5-10% (Deschner et al., 2012; Lothenbach et al., 2016).

XRD data were collected using a PANalytical X'Pert Pro MPD diffractometer equipped with a rotating sample stage in a Θ-2Θ configuration applying CuKα radiation (λ=1.54 Å) at 45mV voltage and 40mA intensity with a fixed divergence slit size and an anti-scattering slit on the incident beam of 0.5° and 1°. The samples were scanned between 5° and 75° 2Θ with a X'Celerator detector.

In addition to typical XRD measurements, X-ray Pair Distribution Function (PDF) analyses were performed. This analysis focusses on the entire signals including Bragg peaks and diffuse scattering. PDF represents the distribution of interatomic distances in a compound, regardless of its crystalline state, determined experimentally by a Fourier transform of the powder pattern. PDF is thus an efficient technique for studying of short coherence lengths materials such as cement (Meral et al., 2011) or geopolymers (White et al., 2013). The reduced PDF, G(r), was obtained by taking a sine Fourier transform of the measured total scattering function S(Q), as shown in equation (2), where Q is the momentum transfer given in equation (3) with θ as the scattering angle and λ as the wavelength of the incident radiation (Egami and Billinge, 2003; White et al., 2013).

$$G(r) = \frac{2}{\pi}\int_{Q_{min}}^{Q_{max}} Q[S(Q) - 1]\sin(Q_r)\, dQ \quad (2)$$

$$Q = \frac{4\pi sin\theta}{\lambda} \quad (3)$$

It is important to obtain diffraction data with a high momentum transfer (Q) in order to maximize the resolution after the Fourier transform. We, therefore, used an X'Celerator Panalytical diffractometer equipped with a Mo source ($\lambda_{k_\alpha} = 0.70926$Å). The powder diffraction pattern was scanned over the 6.004-153.932° angular range with a step size of 0.0083°. The total acquisition was the average of 2 runs recorded over 24 hours. The PDF and standard corrections (Egami and Billinge, 2003) were calculated with PDFGetX2 (Qiu et al., 2004). The density number of atoms ρ_0 used to calculate the PDF was 0.10 atoms $Å^{-3}$. The use of a finite value of Q (17Å) for the PDF analysis led to the addition of spurious oscillations to G(r) depending on the distance r. These oscillations were smoothed by the use of a Lorch (1969) function.

The ^{29}Si MAS NMR experiments were recorded on a Bruker Avance III NMR spectrometer using a 7 mm CP/MAS probe at 79.5 MHz applying the following parameters: 4500 Hz sample rotation rate, minimum of 3072 scans or more, 90° 1H pulse of 7.5 µs, 20 s relaxation delays, RF field strength of 33.3 kHz during SPINAL64 proton decoupling. The ^{29}Si chemical shifts NMR spectra were referenced to the Aldrich external sample of tetramethylsilane (TMS) with a ^{29}Si chemical shift at -2.3 ppm. The observed ^{29}Si resonances were analysed using the Q^n classification, where a Si tetrahedron is connected to n Si tetrahedra with n varying from 0 to 4. The quantification was performed by non-linear least-square fits using the ''DMFIT'' software developed by Massiot et al. (Massiot et al., 2002). Amorphous silica was quantified taking into account the shift at -100.9 ppm (Q^3 from the surface of the amorphous silica (d'Espinose de Lacaillerie et al., 1995; Nied et al., 2016)) and the Q^4 shift at -110 ppm. However, the T_1 relaxation time of amorphous silica can be very long and the amount of amorphous silica might be underestimated.

The deconvolutions of the C-S-H signals were performed following the procedure outlined in literature (Myers et al., 2015), with a constant Lorentzian/Gaussian ratio equal to 0.5 and by keeping the ratio between bridging and pairing silicate tetrahedra constant according to equation (3):

$$\frac{Q^2{}_b + Q^2{}_u}{Q^2{}_p} = 0.5 \quad (3)$$

where Q^2_b is the bridging silicate tetrahedron with one calcium neighbor in the interlayer, Q^2_u is the bridging tetrahedron with one H^+ neighbor in the interlayer and finally Q^2_p is the pairing tetrahedron. The mean chain length (MCL) of the silicate chains in C-S-H was calculated following equation (4):

$$MCL = \frac{2(Q^1 + Q^2{}_b + Q^2{}_u + Q^2{}_p)}{Q^1} \quad (4)$$

The Q^1 and Q^2 environments in M-S-H were deconvoluted using mainly Lorentzian functions while the Q^3 environment was deconvoluted with Gaussian functions following the procedure outlined by (Bernard et al., 2017b). Based on the available M-S-H deconvolutions in literature (Bernard et al., 2017b; Nied et al., 2016; Roosz et al., 2015; Walling et al., 2015), the Q^2/Q^3 ratio was kept between 0.4 and 1.

The TEM characterizations were carried out on a JEOL JEM 2100F microscope operating at 200 kV and fitted out with a Bruker XFlash 5030 for EDS analysis. A few milligrams of powder was vigorously mixed with a few milliliters of pure ethanol in a mortar with a pestle for less than one minute. A TEM carbon-covered cupper grid held with tweezers was then dipped just below the ethanol surface to collect suspended particles on it. The grid was then inserted in the TEM chamber and the vacuum was recovered after about 15 min.

The zeta potential measurements were carried out directly in suspension before filtration with 5 g of solid per 225 mL. The samples were stirred in a beaker at 500 rpm during 10 minutes to reach a stable value before the measurement. During the measurements, they were stirred at 400 rpm and each measurement was repeated 10 times. Zeta potential data were recorded with a ZetaProbe from Colloidal Dynamics Inc., which is based on the frequency-dependent electroacoustic effect. Shortly, an alternating voltage is applied to the suspension which causes charged particles to move back and forth at a mobility that depends on their zeta potential. The software calculates the zeta potential from the frequency-dependent mobility using the O'Brien equation (James et al., 1992). Finally the values obtained were background corrected with a measurement of the filtrated aqueous phase. The zeta potential (-8.1 mV ± 0.9 mV) measured for the C-S-H reference (Ca/Si = 0.8) is consistent with data from the literature (Haas and Nonat, 2015; Labbez et al., 2007; Viallis-Terrisse et al., 2001).

Cation exchange capacity (CEC) in the samples was measured on 100 mg of powder. The cations on the surface and/or from the interlayer were exchanged with cobalt hexamine trichloride during 30 min at room temperature (Jenni et al., 2014) using a solution/solid mass ratio of 30. The suspensions were filtered and the concentrations of Na^+, K^+, Ca^{2+}, Mg^{2+} in solution were determined by ion chromatography (IC) as detailed above. The sum of measured cations was compared to the total CEC which was obtained from the difference in the cobalt hexamine concentration from the original solution and from the leachate. Such concentrations were determined by colorimetry (absorption band at 473 nm) using a UNI-CAM UV visible spectrometer. The good agreement between the total CEC measured by colorimetry and the CEC calculated from the measured cations showed that dissolution of M-S-H and C-S-H was negligible. The Mg_{exch}/Si and the Ca_{exch}/Si (Cat_{exch}/Si) were calculated from the CEC measurement following the equation (5):

$$\frac{Cat_{exch}}{Si} = \frac{\text{Cation (CEC)}}{0.1/M} \quad (5)$$

where Cation (CEC) is the mol of cations (magnesium or calcium) obtain by the CEC (IC), the 0.1 corresponds to the 0.1 g of solid used in the CEC measurement and M is the molar mass in g/mol of the phase corresponding ($M_{0.8}SH_{1.5}$ or $M_{0.75}C_{0.05}SH_{1.5}$ for example).

The solids were washed after the CEC and dissolved in 0.1 mol/L HCl to investigate whether any calcium remained in the M-S-H after the exchange with the cobalt hexamine. The solutions were analyzed by ICP-MS with Agilent triplequad MS (Agilent 8900 QQQ ICP-MS). Sodium and magnesium concentrations have been measured in the "NoGas" mode while the calcium concentration has been measured in the "Helium" mode. It might be that calcium was slightly overestimated due the presence of residual calcium from the exchange. ICP-MS had been used as in IC it was not possible to detect small calcium concentrations in the presence of high magnesium concentrations.

2.3. Thermodynamic modelling

Thermodynamic modelling of the experiments was carried out using the Gibbs free energy minimization program GEMS (Kulik et al., 2013). GEMS is a broad-purpose geochemical modelling code which computes equilibrium phase assemblage and speciation in a complex chemical system from its total bulk elemental composition. The thermodynamic data for aqueous species as well as for brucite and portlandite were taken from the PSI-GEMS thermodynamic database (Thoenen et al., 2014). The amorphous SiO_2 data were from Bernard et al. (2017b).

The ion activity products (IAP) were calculated from the measured composition of the solutions for all the samples with respect to $M_{0.78}SH_{1.48}$ and $C_{0.80}SH_{1.94}$ to observe whether any change occurred upon variation of the pH and/or the concentration of other species.

The solubility of low-crystalline phases with variable composition such as C-S-H and M-S-H can be described either by solid solutions, which allow a continuous change of composition of the solid, or by defining solubility products for a range of possible compositions leading to a large number of different solubility products (as has been done e.g. by Dauzères et al., 2016; Gaucher et al., 2004; Trapote-Barreira et al., 2014). If single solubility products are used the resulting aqueous concentrations or solid compositions are described by steps as shown in e.g. (Nied et al., 2016), while a solid solution approach, which defines only the solubility products of end-members solids, allows describing gradual changes in the C-S-H or the M-S-H composition and in the aqueous phases (for more detailed see (Bernard et al., 2017b; Kulik, 2011; Nied et al., 2016)). The solid solution models used have been developed for C-S-H with $0.67 < Ca/Si < 1.5$ by Kulik (2011) and M-S-H with $0.78 < Mg/Si < 1.3$ (Bernard et al., 2017b).

The thermodynamic data used of the solid solutions of M-S-H (defined by two end-members) and of C-S-H (defined by three end-members), and of brucite, portlandite, and amorphous silica are summarized in Table 2.

Based on the experimental observations (as presented below in Results and discussions), M-S-H phases containing small amounts of calcium were defined. The solubility products of two possible end-members, $M_{0.68}C_{0.1}SH_{1.48}$ and $M_{1.2}C_{0.1}SH_{1.80,}$ were fitted using the measured concentrations and implemented in the solid solution model of M-S-H as detailed in Table 2. The formation of an ideal solid solution between the 4 endmembers ($M_{0.78}SH_{1.48}$, $M_{1.3}CSH_{1.80}$, $M_{0.68}C_{0.1}SH_{1.48}$ and $M_{1.2}C_{0.1}SH_{1.80}$) was assumed.

Table 2: Standard thermodynamic properties at 25 °C and P = 1 atm.

	*	$LogK_{S0}$ [a]	$\Delta_f G°$ [kJ/mol]	V° [cm^3/mol]	density [g/cm^3]	Ref.
Brucite	MH	-11.16	−832.23	24.6	2.37	(Thoenen et al., 2014)
Portlandite	CH	-5.2	−897.01	33.1	2.24	(Thoenen et al., 2014)
SiO_2,am	S	-2.9	-849.9	29	2.07	(Bernard et al., 2017b)
M-S-H						
Mg/Si = 0.78	$M_{0.78}SH_{1.48}$	-14.59	-1682.2	56	2 [b]	(Bernard et al., 2017b)
Mg/Si=1.30	$M_{1.30}SH_{1.80}$	-21.44	-2073.5	72	2 [b]	(Bernard et al., 2017b)
Mg/Si = 0.68 Ca/Si = 0.10	**$M_{0.68}C_{0.1}SH_{1.48}$**	**-14.42** [c]	-1689.7	57	2 [b]	this
Mg/Si = 1.20 Ca/Si = 0.10	**$M_{1.20}C_{0.1}SH_{1.80}$**	**-21.57** [c]	-2082.0	73	2 [b]	study
C-S-H						
Ca/Si = 0.67	$C_{0.67}SH_{1.67}$	-10.24	-1707.3	56.6	2.25	(Kulik, 2011)
Ca/Si = 1.0	$C_{1.00}SH_{2.00}$	-13.41	-2014.5	63.4	2.4	(Kulik, 2011)
Ca/Si = 1.5	$C_{1.5}SH_{2.50}$	-16.61	-2466	80.6	2.35	(Kulik, 2011)

**cement shorthand notations: C= CaO; H =H_2O; M = MgO; S = SiO_2*

[a] *all solubility products refer to the solubility with respect to the species Mg^{2+}, Ca^{2+}, SiO_2^0, OH^-, or H_2O*

[b] *estimated from M-S-H volumes*

[c] *values at 20°C.*

3. Results and discussions

3.1. Co-0.05 and Co-0.10 samples

This section focusses on M-S-H syntheses labelled Co-0.05 and Co-0.10. The (Mg+Ca)/Si ratio was set to 0.8 and a small fraction of MgO was substituted by CaO (Ca/Si=0.05 and 0.10).

3.1.1. Aqueous phase composition

The pH values and measured concentrations of the solutions equilibrated with the co-precipitated samples are plotted in Figure 1 and compared to the data obtained for pure M-S-H and C-S-H.

In the solution at equilibrium with the pure M-S-H sample, a pH of 8.3 was measured, together with magnesium and silicon concentrations of 0.38 mmol/L and 1.44 mmol/L respectively. The substitution of magnesium by calcium at constant (Mg+Ca)/Si ratio of 0.8 increased the pH (Figure 1, Appendix A) from 8.3 to 8.9 (sample Co-0.05) or 9.3 (sample Co-0.10). At the same time, the magnesium concentration was lowered. A comparable decrease of magnesium has been observed for pure M-S-H at higher pH values (Bernard et al., 2017b; Nied et al., 2016) and for M-S-H in the presence of some calcium (Lothenbach et al., 2015). Little difference was observed in the concentrations and pH values between 1 and 2 years confirming that the samples were very close to equilibrium.

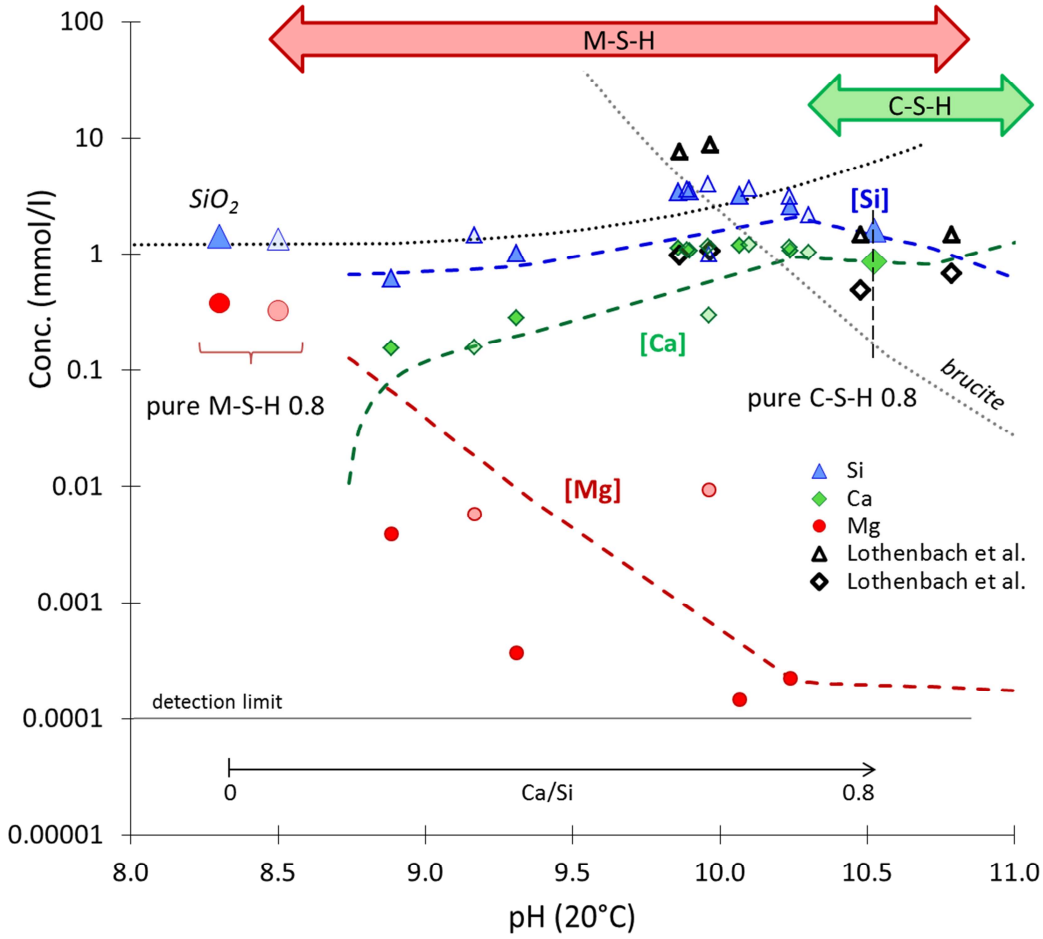

Figure 1: Measured silicon (triangles), magnesium (circles), and calcium (diamonds) concentrations at 20°C at 1 year (lighter symbols) and 2 years (full symbols) as a function of pH. Empty symbols are from Lothenbach et al. (Lothenbach et al., 2015). The solubility of M-S-H, C-S-H (dashed lines), brucite and amorphous silica (dotted lines) were calculated from the thermodynamic data (solid solutions for M-S-H and C-S-H) detailed in Table 2 without considering the formation of mixed M-(C)-S-H phase.

C-S-H phases are not stable at this range of pH (<9.5) (Bernard et al., 2017a; Leisinger et al., 2014; Peyronnard et al., 2009; Shi and Stegemann, 2000; Swanton et al., 2016). It can be noted however that the calcium concentrations were much lower (0.15 to 0.46 mmol/L, depending on the initial calcium content, temperature and time) than the total amount of calcium that could theoretically be present in solution (11.93 ± 1.50 and 23.66 ± 2.60 mmol/L), which suggests the uptake of calcium by the solid phases.

3.1.2. Solid phase analysis

The solid analysis focused on the samples equilibrated for 1 year at 50°C. However, similar results were obtained for the samples equilibrated for 2 years at 20°C indicating that the equilibrium was reached in both conditions (see Appendix A).

The XRD patterns of the two co-precipitated (Co-0.05 and Co-0.10) samples are compared to those of M-S-H and C-S-H in Figure 2. The broad peaks at 19.7, 26.7, 35.0, 60.3° 2Θ (Nied et al., 2016) were attributed to M-S-H, the main phase observed in the samples. In addition, traces of calcite ($CaCO_3$, PDF-00-005-0586) and brucite ($Mg(OH)_2$, PDF-01-083-0114) were present. Their amount was less than 1%, as assessed from TGA (Figure 3).

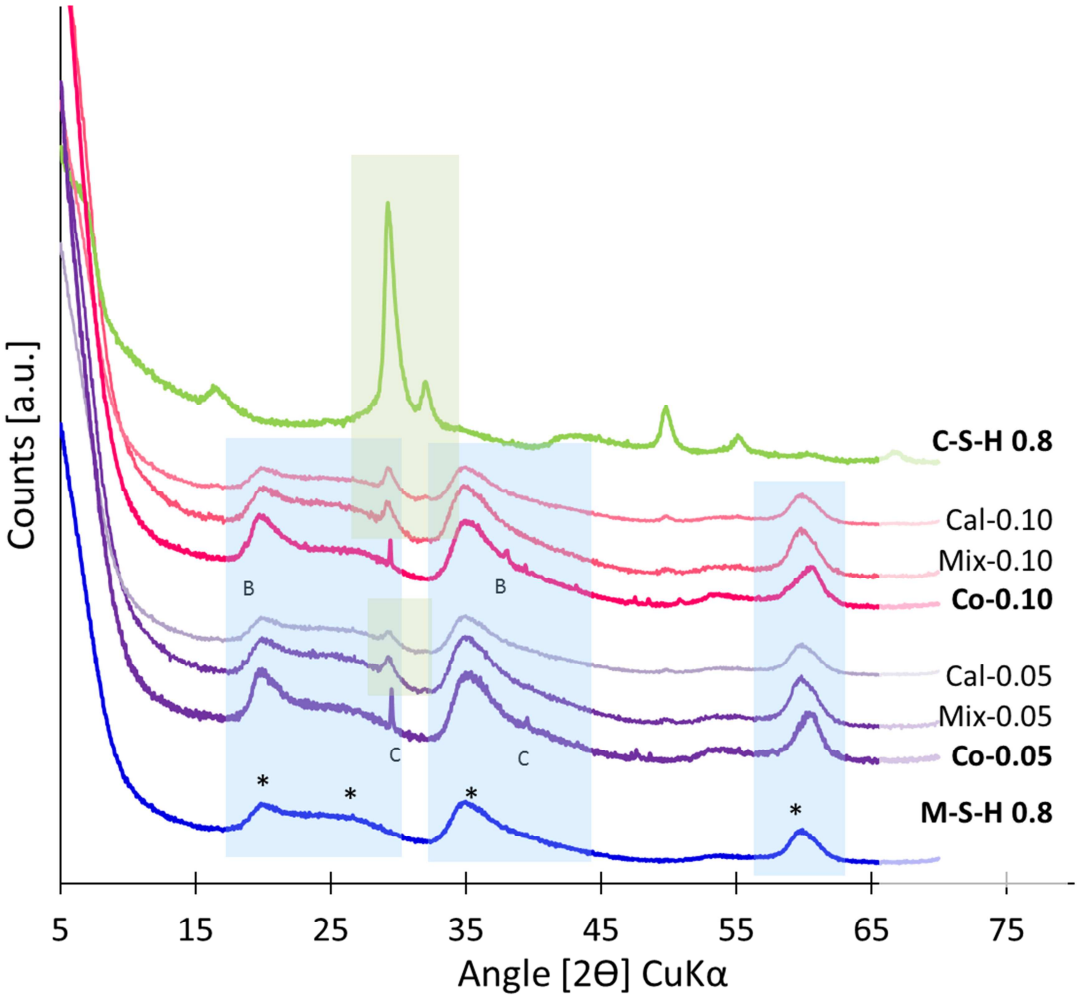

306

307 *Figure 2: XRD patterns of samples Co-0.05 and Co-0.10 after 1 year of curing at 50°C compared to XRD patterns of M-S-H*
308 *0.8 (1 year at 50°C), C-S-H 0.8 (1 year at 50°C) , mixed samples (0.10mix and 0.05mix), calculated reference patterns (Cal-*
309 *0.05 and Cal-0.10) B=$Mg(OH)_2$ (brucite); C= $CaCO_3$ (calcite).*
310

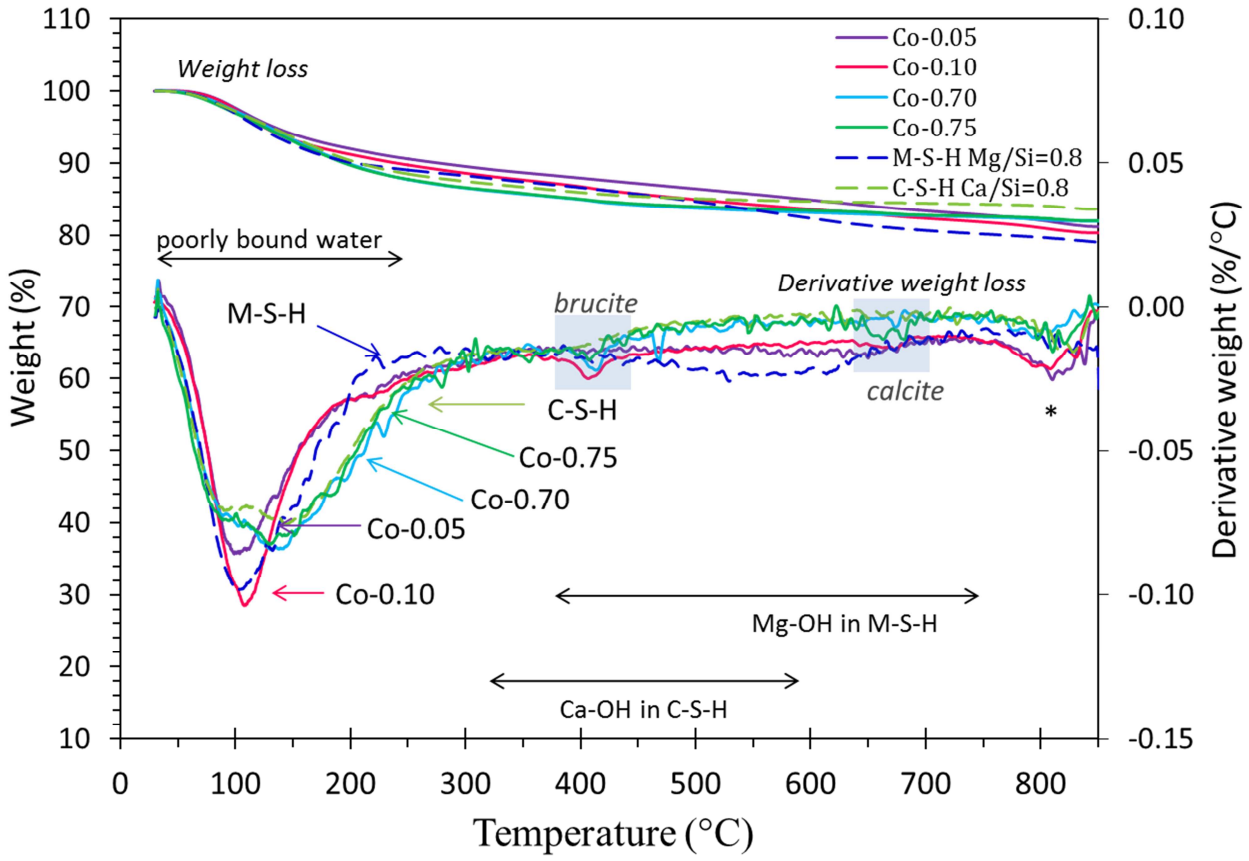

*Figure 3: Thermogravimetric analysis of co-precipitated samples after 1 year of curing at 50°C compared to TGA of C-S-H 0.8 and M-S-H 0.8 (1 year, 50°C), * indicates the formation of wollastonite from C-S-H (Martin et al., 2017) and enstatite from M-S-H (as observed from talc (MacKenzie and Meinhold, 1994)).*

Complementary XRD patterns were measured and calculated for mixes of separately synthesized M-S-H and C-S-H phases. These mixes (Mix-0.05 and Mix-0.10) contained the same Mg/Si and Ca/Si ratios than samples Co-0.05 and Co-0.10, but the presence of any magnesium calcium silicate hydrate (M-C-S-H) could be excluded. The calculated XRD patterns (Cal-0.05, Cal-0.10) resulted from linear combinations of the patterns of plain M-S-H and C-S-H respecting the Mg/Si and Ca/Si ratios. Mix-0.05 and Mix-0.10 samples exhibited the same XRD patterns as the calculated ones (Figure 2), but slight differences were noticed for the co-precipitated samples. C-S-H, characterized by a main reflection peak

323 at ~ 29.2° 2Θ, was present in the separately mixed samples but not in the co-precipitated ones. The sole
324 observation of M-S-H by XRD was in good agreement with the low pH of the solution which should
325 prevent the precipitation of C-S-H. The main part of the calcium initially added was thus neither present
326 in the solution nor in C-S-H (or only in very small quantities not observable by XRD).

327 The reflection at approx. 60.3° 2Θ in pure M-S-H is shifted to 60.4 and 60.5° 2Θ in the Co-0.05 and Co-
328 0.10 samples, respectively. The reflection at higher angles is usually rather characteristic for talc
329 structure, i.e. for a low Mg/Si (0.75) phyllosilicate.

330 ^{29}Si MAS NMR spectra of the co-precipitated samples are presented together with the calculated spectra
331 of the linear combination of pure M-S-H and C-S-H in Figure 4. Pure M-S-H 0.8 usually contains a
332 small amount of amorphous silica (3-5% of SiO_2) (Bernard et al., 2017b; Nied et al., 2016) with a
333 resonance at -110 ppm (Q^4) and a resonance at -100.9 ppm Q^3(-OH) (d'Espinose de Lacaillerie et al.,
334 1995; Nied et al., 2016). The comparison of the calculated spectra with those of samples Co-0.05 and
335 Co-0.10 shows the absence of amorphous silica in the co-precipitated samples.

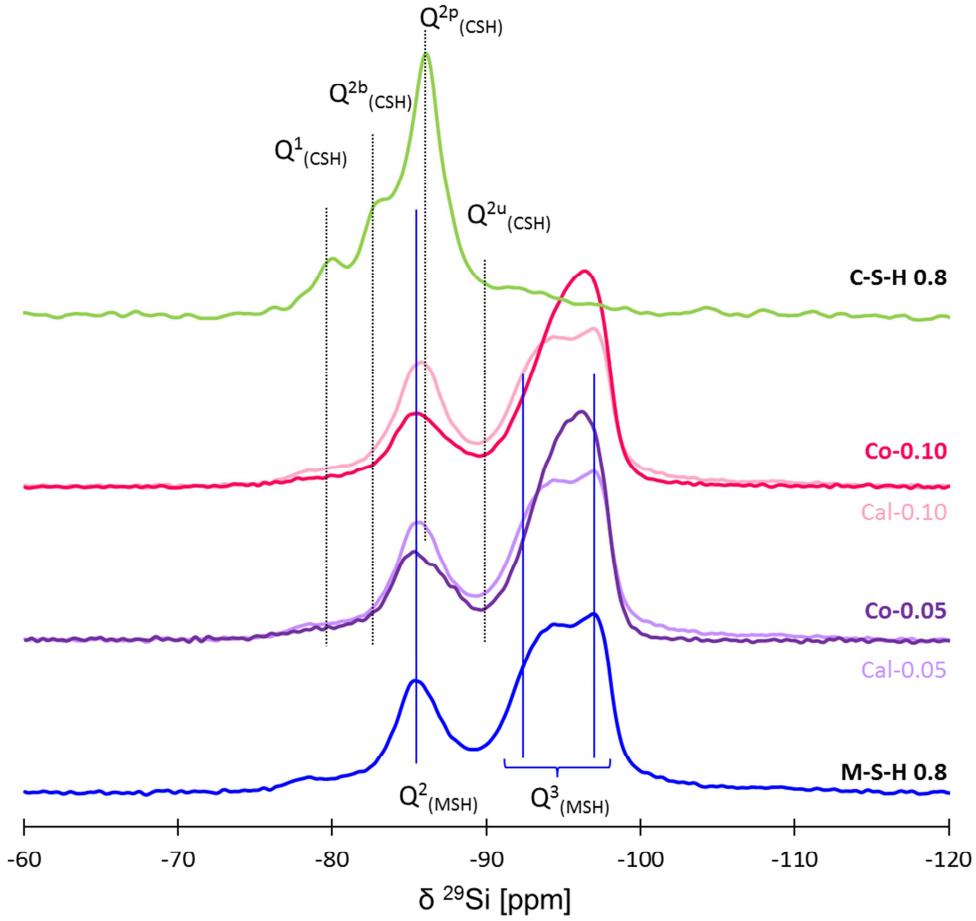

Figure 4: ^{29}Si MAS NMR spectra of Co-0.05 and Co-0.10 samples (1 year at 50°C) compared to spectra of C-S-H 0.8, M-S-H 0.8 and calculated reference samples Cal-0.05 and Cal-0.10.

The ^{29}Si MAS NMR spectra of Co-0.05 and Co-0.10 samples were similar to that of M-S-H 0.8 (Figure 4) with the presence of Q^2 tetrahedral silicate (chemical shifts at approx. -85.6 ppm) and Q^3 tetrahedral silicate (chemical shift between -92 and -97 ppm (Brew and Glasser, 2005; d'Espinose de Lacaillerie et al., 1995; Nied et al., 2016; Roosz et al., 2015; Walling et al., 2015)). No C-S-H could be detected. The comparison with the calculated spectra in Figure 4 points out a lower intensity of the Q^2 signal, but a higher content of Q^3 species. The Q^2 signal was broader and the Q^3 signal was less symmetrical and shifted to slightly more negative chemical shifts. This would be consistent with the presence of calcium

in the vicinity of silicon since calcium shields silicon stronger than magnesium (Lothenbach et al., 2015; Mägi et al., 1984).

The associated deconvolutions are detailed in Table 3. The spectra were deconvoluted based on the deconvolution of pure M-S-H (Bernard et al., 2017b; Brew and Glasser, 2005; Nied et al., 2016). The fraction of Q^3 silicate sites in M-S-H 0.8 (61% ±7%) increased to 73% (±8%) in Co-0.05 and Co-0.10 samples. The Q^2/Q^3 ratio calculated in the co-precipitated samples of ~0.4 (Table 3) was lower than the 0.6 usually found in pure M-S-H 0.8 (Bernard et al., 2017b). As the Q^2/Q^3 in M-S-H decreases with the decrease of Mg/Si (Bernard et al., 2017b), this low Q^2/Q^3 ratio suggests that the co-precipitated samples might have a Mg/Si lower than 0.8 (approx. to 0.7-0.75). The higher polymerization of the silicate network in the co-precipitated sample, together with the shift observed by XRD at high angles, seems to indicate a lower content of magnesium rather than the presence of calcium in the octahedral layers and thus that calcium might rather be adsorbed than incorporated in the octahedral layers. This is further investigated by complementary analyses.

Table 3: Relative peak area of the different silicon chemical shifts obtained from the deconvolution of the ^{29}Si MAS NMR spectra for the co-precipitated samples after 1 year of curing at 50°C (C-S-H (1 year at 20°C) and M-S-H (1 year at 50°C) shown as references).

	C-S-H				MCL	M-S-H							% of Si in		
	Q^1	Q^2_b	Q^2_p	Q^2_u	Q^3(?)	Q^1	Q^2	Q^3_a	Q^3_b	Q^3_c	App. Q^2/Q^3	$Q^3(SiO_2)$	C-S-H	M-S-H
	-79.6	-82.8	-85.8	-88.2	-93.5	-78.3	-85.5	-92.7	-94.7	-96.7		-100.9		
M-S-H 0.8	-	-	-	-	-	1	35	24	10	28	0.6	3	-	97
Co-0.05	-	-	-	-	-	1	27	18	25	29	0.4	-	-	100
Co-0.10	-	-	-	-	-	1	27	17	28	28	0.4	-	-	100
Co-0.70	6	17	42	3	23	3	0	9	8	5	7	0.4	0	69	28
Co-0.75	7	19	47	5	22	3	0	5	5	3	5	0.4	1	78	18
C-S-H 0.8	8	22	59	7	25	4	-	-	-	-	-	-	-	96	-

Error = ± 8% of absolute amounts of (%Si) + 2.5%.

The decrease in the fraction of Q^2 sites (resonance at -85.6 ppm) from 35±5% in M-S-H 0.8 to 27±4% for the co-precipitated samples (Co-0.05 and Co-0.10) also confirmed the absence of any significant

367 amount of C-S-H (comparison between Co-0.05 and Co-0.10 and the calculated spectra in Figure 4),
368 which was consistent with their characterization by XRD and with the low pH of their solution, outside
369 the stability domain of C-S-H. ^{29}Si MAS NMR thus confirmed that the fraction of calcium in the solid
370 phase was not precipitated as C-S-H.

371 Additional characterizations of M-S-H 0.8, C-S-H 0.8, Co-0.05 and Co-0.10 solid fractions were
372 performed using X-ray pair distribution function (PDF) analysis (Figure 5a). The X-ray PDF analysis of
373 pure M-S-H 0.8 indicated a structure where magnesium was bound to silicon and hydroxide.

374 The X-ray PDF analysis of M-S-H 0.8, Co-0.05 and Co-0.10 samples were very similar, and
375 significantly different from that of C-S-H (Figure 5a), which confirmed again that the products formed
376 using the co-precipitation method had a M-S-H structure. The structural correlation peaks could be
377 tentatively assigned using the structure of talc as a reference (Gruner, 1934): they mainly corresponded
378 to Mg-Mg distances (r = 3.13 Å, 5.36 Å, 8.21 Å, 9.42 Å, 11.06 Å) and Mg-O (2.03 Å) within a same
379 layer as well as Si-Si (3.20 Å) and Si-O distances in silicate tetrahedra (r =1.61 Å). Two additional
380 peaks at r = 2.41 Å and 7.06 Å might be observed in the presence of calcium. The first distance is related
381 Ca-O distances in the solid (detailed below). The peak at 2.4 Å would indicate the presence of CaO_7
382 polyhedra (Skinner et al., 2010) as also present in C-S-H or in other octahedral layer minerals such as
383 e.g. dolomite or tobermorite, indicating either the presence of small quantities of C-S-H or the
384 incorporation of some calcium in the octahedral layers of M-S-H.

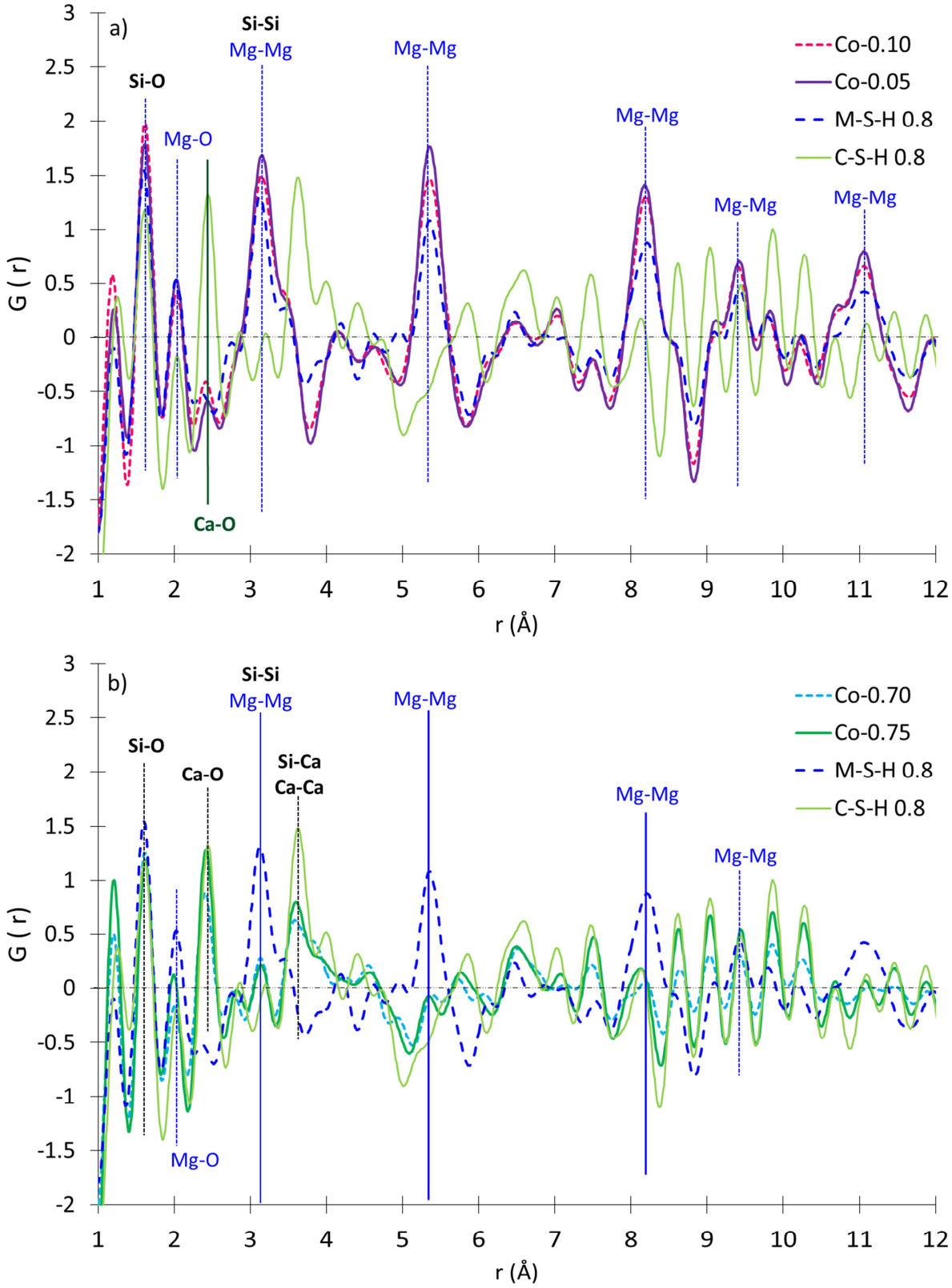

Figure 5: Reduced pair distribution function of M-S-H, C-S-H compared to a) co-precipitated Co-0.05 and Co-0.10 samples and to b) co-precipitated Co-0.70 and Co-0.75 samples.

3.1.3. Surface properties

The zeta potential of M-S-H 0.8, M-S-H 1.0 and of the co-precipitated samples (cured during 2 years at 20°C) are plotted versus the calcium concentrations in solution in Figure 6a and versus the magnesium concentrations in solution in Figure 6b. After 2 years, the less than 2 wt. % of brucite is present (see Appendix A**Error! Reference source not found.**); such a low amount would not affect the zeta potential measured. The effective surface charge of M-S-H was negative with zeta potential values between -19 ± 3 mV and -25 ± 3 mV depending on the pH of the solution (within the pH range 8.3 - 9.2).

The substitution of MgO by CaO increased the pH from 8.3 to 8.9 and 9.3 for Co-0.05 and Co-0.10 samples respectively. This pH increase will thus lead to more negatively charge silanol groups of the Q^1 & Q^2 silicon species at the surface and edge sites of M-S-H, and should result in an increase of the negative surface charge density.

At the same time, the calcium concentration in solution increased from 0 to 0.15 and 0.29 mmol/L respectively and the magnesium concentration in solution dropped from 0.38 to 0.004 and below the detection limit of 0.001 mmol/L respectively. The Co-0.05 sample exhibited almost the same zeta potential as pure M-S-H with – 22 ± 3 mV at pH 8.9, which is an intermediate value between the two points of pure M-S-H (in zeta potential as well as in pH) whereas the zeta potential of the Co-0.10 sample was significantly less negative (-10 ±1 mV). The surface charge of M-S-H thus depended on the calcium concentration as shown in Figure 6a. As in the case of C-S-H (Haas and Nonat, 2015; Labbez et al., 2007; Labbez et al., 2011; Plusquellec and Nonat, 2016; Viallis-Terrisse et al., 2001), the zeta potential became less negative at higher concentration of dissolved calcium, indicating a sorption of calcium at the surface. One may postulate that, in the case of Co-0.05 sample, calcium substituted a similar amount of magnesium at the surface, resulting in little change of the zeta potential. The strong

412 increase in the zeta potential of the second sample (Co-0.10) would indicate that calcium was more
413 effectively adsorbed at the surface of M-S-H than magnesium, thus partially compensating the negative
414 charge of the silicate sites.

415 The magnesium concentration in solution did not seem to influence the zeta potential of M-S-H as
416 strongly as the calcium concentration, as shown in Figure 6b. In this Figure, we can see no influence of
417 the magnesium concentration on the effective negative surface of M-S-H. Calcium has been observed to
418 sorb stronger than magnesium on quartz (Conway, 1981; Dove and Nix, 1997) probably due its slight
419 smaller hydrated size. Such a preferential sorption of calcium could explain the strong increase in zeta
420 potential when the calcium concentration increased.

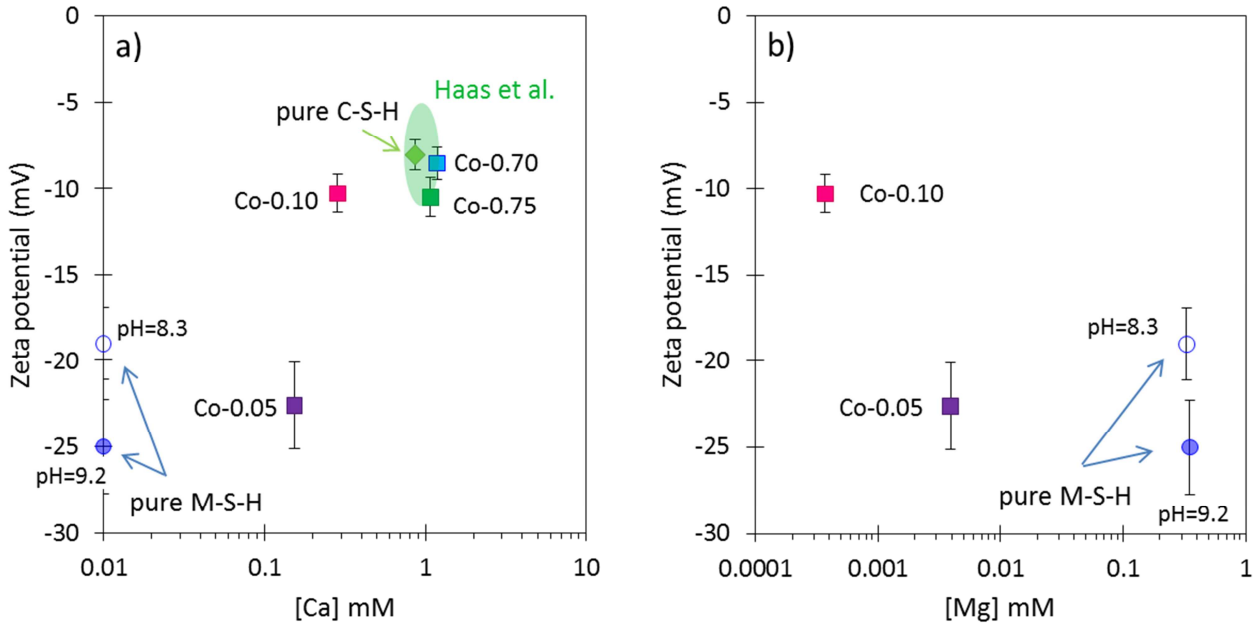

421

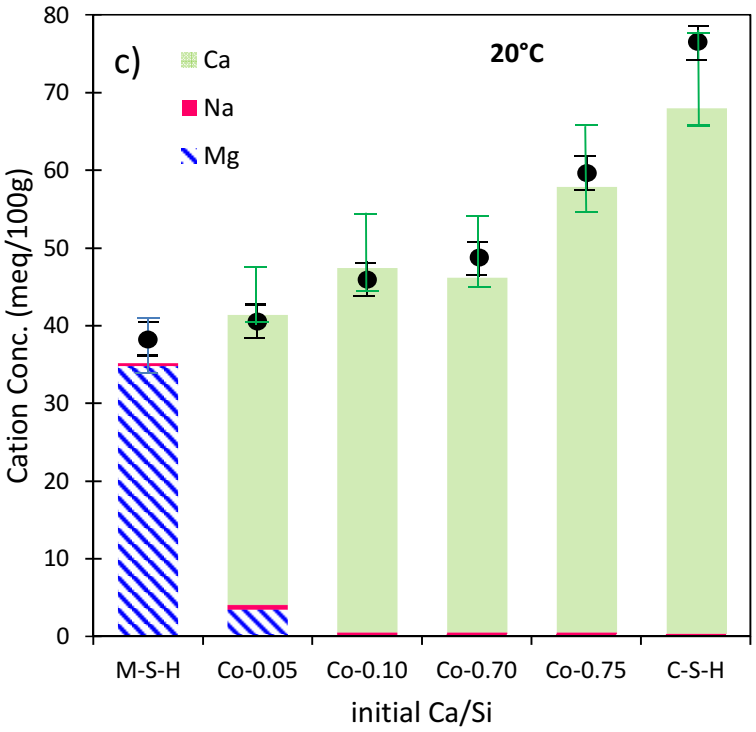

422

423 *Figure 6: Zeta potential of M-S-H, co-precipitated sample particles a) versus calcium concentration in suspension (range*
424 *of values for C-S-H from Haas et al. (Haas and Nonat, 2015) added for comparison) and b) versus magnesium*
425 *concentration; c) Concentrations of the cations sorbed on co-precipitated samples compared to M-S-H 0.8 and C-S-H 0.8*
426 *measured by the cobalt hexamine method as a function of the initial Ca/Si. CEC measurements by colorimetry (black*
427 *circles) have been added for comparison.*

428

429 The measurement of the cation exchange capacity of M-S-H showed a positive CEC of 35 meq/100g
430 (Figure **6**c), which indicated a negative surface charge of the M-S-H particle. This is in agreement with
431 the effective negative surface charge obtained by zeta potential measurement. The exchangeable
432 magnesium in pure M-S-H 0.8 was calculated following the equation (5) and was equal to 0.02 per
433 silicon. The CEC of the Co-0.05 and Co-0.10 samples was slightly higher in the presence of calcium. It
434 increased from 35 meq/100g to 47 meq/100g for Co-0.10 sample. This sample, thus, contained slightly
435 more exchangeable calcium, about 0.03 per silicon. In the Co-0.05 sample, most of the magnesium at
436 the surface was replaced by calcium (Figure 6c and Table 4) and all of it in the Co-0.10, in agreement

437 with the much higher calcium concentration than magnesium one in solution. The general CEC increase
438 from the pure M-S-H to the Co-0.05 and Co-0.10 indicates a more negative surface charge.

439 *Table 4: Exchangeable magnesium and calcium per silicon in co-precipitated samples compared to M-S-H 0.8 and C-S-H*
440 *0.8 calculated from CEC*

sample	exchangeable Mg^{2+} per Si	exchangeable Ca^{2+} per Si	total
M-S-H	0.021	--	0.021
Co-0.05	0.002	0.022	0.024
Co-0.10	<0.001	0.028	0.028
Co-0.70	<0.001	0.032	0.032
Co-0.75	<0.001	0.040	0.040
C-S-H	<0.001	0.048	0.048

441

442 The uptake of 0.022 and 0.028 Ca_{exch}/Si (CEC in Table 4) at exchangeable sites compared to the total
443 calcium uptake of 0.05 and 0.10 Ca/Si (if all the initially added calcium would be on CEC sites in the
444 solid) showed that only a part of calcium was found adsorbed at the surface of M-S-H.

445 To confirm that, CEC was also measured at room temperature on the samples synthesized at 50°C.
446 Similar results were obtained with Ca_{exch}/Si ratios of 0.03 and 0.04 at CEC sites in the Co-0.05 and Co-
447 0.10 samples (**Error! Reference source not found.** & **Error! Reference source not found.**).

448 The remaining calcium may substitute some magnesium in the octahedral layer. Although substitution of
449 magnesium by calcium (with a bigger size) is unusual, it might occur during co-precipitation within the
450 poorly ordered M-S-H.

451 Alternatively, a part of calcium might have been washed during the filtration process. To check whether
452 calcium was still present in the solid phase (i.e. in the octahedral layers) after the CEC and to account
453 for the missing calcium, the co-precipitated samples after cation exchange by cobalt hexamine
454 trichloride were dissolved in 0.1 mol/L HCl, to differentiate between surface-sorbed calcium
455 (determined by CEC measurement) and calcium in the structure. As the CEC measurement should

remove the surface-sorbed calcium, any calcium still found is present as non-exchangeable. $Ca_{not\ exch}/Si$ ratios of 0.02 and 0.05 were measured in the solids after dissolution (Table 5), confirming the presence of calcium in the solid part and the total Ca/Si found by the addition of the Ca_{exch}/Si and $Ca_{not\ exch}/Si$ was approximatively equal to the initial Ca/Si added to the suspensions.

Table 5: Ca/Si and Mg/Si in the solids synthesized at 50°C from mass balance and dissolution, before and after the CEC.

	Mass balance		Dissolution		
			Before CEC	After CEC	**Not exchangeable cation***
	Ca/Mg	Mg/Si	Ca/Mg	Ca/Mg	**Ca/Si***
Co-0.05	0.06±0.02	0.76±0.02	0.07±0.02	0.03±0.01	**0.02±0.02**
Co-0.10	0.14±0.02	0.71±0.02	0.13±0.02	0.08±0.02	**0.05±0.02**

**Ca/Si=Ca/Mg (after CEC) x Mg/Si (Mass balance).*

In summary, the different analyses indicated an adsorption of calcium on the surface of M-S-H; a small calcium uptake in the M-S-H main layers might occured; alternatively a small amount of C-S-H could be present although this seemed unlikely due to the low pH value and based on different solid analyses. Thus, M-(C)-S-H corresponds to a M-S-H phase containing small quantities of adsorbed and/or incorporated calcium. The exact nature of calcium incorporation, however, still remains unclear.

3.2. Co-0.75 and Co-0.70 samples

This second section investigates the effect of small amounts of MgO (Mg/Si=0.05 and 0.10) added during the synthesis of C-S-H. The (Ca+Mg)/Si ratio was set to 0.8, and the resulting samples were labelled Co-0.75 and Co-0.70.

3.2.1. Aqueous phase composition

The aqueous phase equilibrated with pure C-S-H (Ca/Si ratio of 0.8) exhibited a pH of 10.5 and dissolved calcium and silicon concentrations of 0.86 mmol/L and 1.62 mmol/L respectively (Figure 1, Appendix A). These results are in good agreement with previously reported data (Lothenbach and Nonat, 2015). At the later age (2 years at 20°C where only traces of brucite were present, see Appendix

476 A), the partial replacement of CaO by MgO in Co-0.75 and Co-0.70 samples caused a decrease in pH to
477 10.2 and 10.1 respectively, and an increase in the calcium and silicon concentrations.

478 The higher pH values resulted in very low concentrations of magnesium in solution (Figure 1, Appendix
479 A), as also observed when only M-S-H is formed at pH 10 (Bernard et al., 2017b; Zhang et al., 2011).
480 The high pH and the very low concentration of magnesium tentatively indicated the presence of both M-
481 S-H and C-S-H.

482 **3.2.2. Solid analysis**

483 The solid analysis focused on the samples synthesized 1 year at 50°C; similar analyses were done on the
484 samples synthesized 2 years at 20°C and only traces of brucite were present in both cases.

485 Since the formation of M-S-H is very slow at 20°C, especially at high pH (Lothenbach et al., 2015), the
486 presence of brucite ($Mg(OH)_2$) was observed up to 1 year (Appendix A). After 2 years however, only
487 traces of brucite were detected. The samples cured at 50°C reacted faster and equilibrium was reached
488 after 1 year.

489 The XRD patterns of Co-0.75 and Co-0.70 samples are compared to pure C-S-H pattern in Figure 7. C-
490 S-H was the main phase present in these samples. However, a small amount of M-S-H (10-20wt.%) is
491 difficult to detect by XRD in the presence of C-S-H (Bernard et al., 2017a). As for the magnesium co-
492 precipitated samples (see 3.1.), complementary XRD patterns were measured and calculated to make the
493 comparison easier. Some reference samples (Mix-0.75 and Mix-0.70) were prepared by mixing pure M-
494 S-H and C-S-H phases with total (Mg+Ca)/Si ratios corresponding to those of experiments Co-0.75 and
495 Co-0.70. Their diffraction patterns were recorded and calculated by linear combination of the patterns of
496 plain M-S-H and C-S-H (Cal-0.75 and Cal-0.70). The calculated and separately mixed samples showed
497 the same reflections. Similarly, all the patterns exhibited almost the same diffraction patterns and M-S-H

498 phases were very difficult to observe. The co-precipitated samples could thus contained small amounts
499 of M-S-H, but other characterizations were needed to ascertain the presence of this phase.

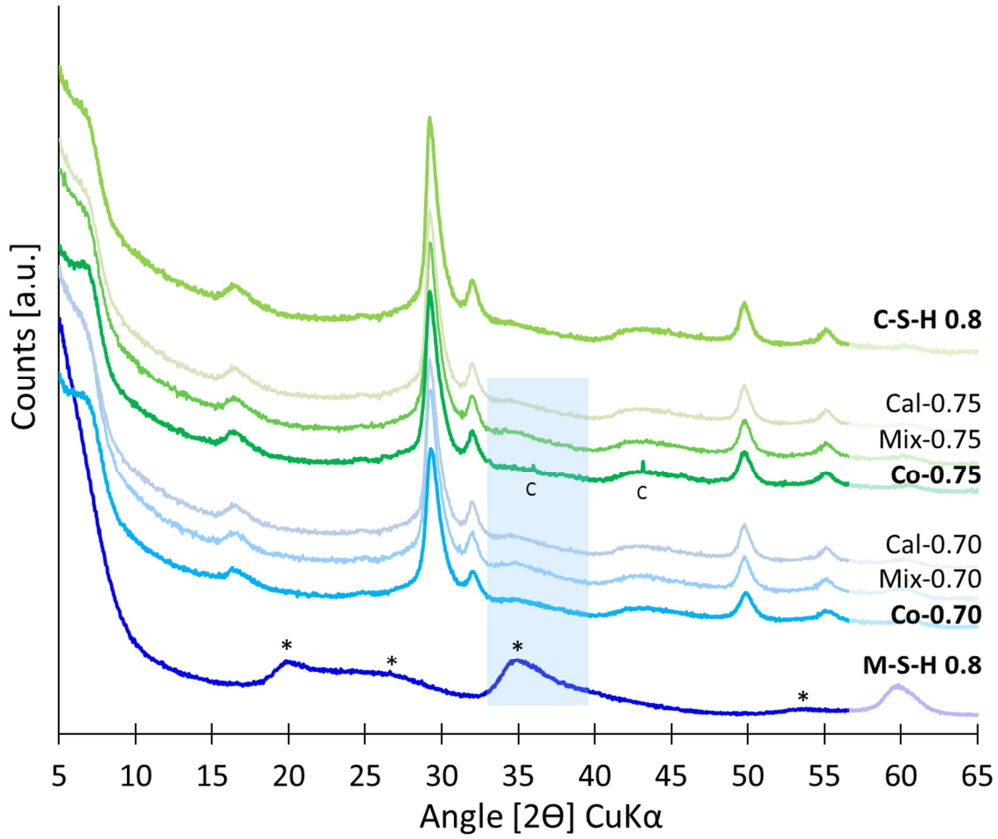

500

501 *Figure 7: XRD patterns of Co-0.70 and Co-0.75 samples (1 year at 50°C) compared to XRD patterns of C-S-H 0.8, M-S-H 0.8*
502 *and calculated and mechanically mixed samples. C=calcite, *=M-S-H.*

503

504 The X-ray PDF of Co-0.70 and Co-0.75 and C-S-H (Figure 5b) bore strong resemblance. According to
505 the literature (Grangeon et al., 2013; Lequeux et al., 1999; Meral et al., 2011; Skinner et al., 2010;
506 White, 2016; White et al., 2015), the correlations peaks might correspond to Si-O distances (r = 1.61 Å
507 and 3.63 Å), Ca-O distances (r = 2.44 Å), Ca-Ca distances (r = 3.80 Å and 6.63 Å) Si-Ca distances (r =
508 3.20 Å and 3.63 Å) and possibly Si-Si distances (r = 3.20 Å). Small differences were however noticed
509 between the pure C-S-H and the co-precipitated samples: the correlation peaks observed at r = 3.14 Å

510 and 5.38 Å in the co-precipitated samples were characteristic of Mg-Mg distances observed in M-S-H.
511 The intensity of the correlation peaks assigned to Ca-Ca distances was also lower. These results might
512 suggest the presence of small amounts of M-S-H in the co-precipitated samples, but this again needed to
513 be confirmed by other techniques.

514 The ^{29}Si MAS NMR spectra of the co-precipitated samples (Co-0.75 and Co-0.70) are shown in Figure
515 8. ^{29}Si MAS NMR data confirmed the presence of C-S-H with typical chemical shifts (Andersen et al.,
516 2003; Bell et al., 1990; Chen et al., 2004; Klur et al., 1998; L'Hôpital et al., 2015; Richardson et al.,
517 2010) at approx. -79.7, -82.9, -85.8 and -88.4 ppm corresponding to Q^1 (end of chains), Q^2_b (bridging
518 position), Q^2_p (pairing position) and Q^2_u (bridging position with binding to H^+ (L'Hôpital et al., 2015; Le
519 Saout et al., 2006; Sato and Grutzeck, 1991)) of the silicate tetrahedra in C-S-H, as shown in Figure 8.
520 The pure C-S-H sample with a Ca/Si ratio of 0.8 contained mainly Q^2 species, and only very small
521 amounts of Q^3 species (broad signal at -93.5 ppm which accounted for ≃ 4% of the total silicate), in
522 agreement with previous studies of C-S-H with low Ca/Si ratio (Le Saout et al., 2006; Myers et al.,
523 2015). The presence of M-S-H in the samples was evidenced by the presence of the resonance peaks
524 between -92 and -97 ppm corresponding to Q^3 tetrahedral sites of M-S-H (Brew and Glasser, 2005;
525 d'Espinose de Lacaillerie et al., 1995; Nied et al., 2016; Roosz et al., 2015; Walling et al., 2015).

526

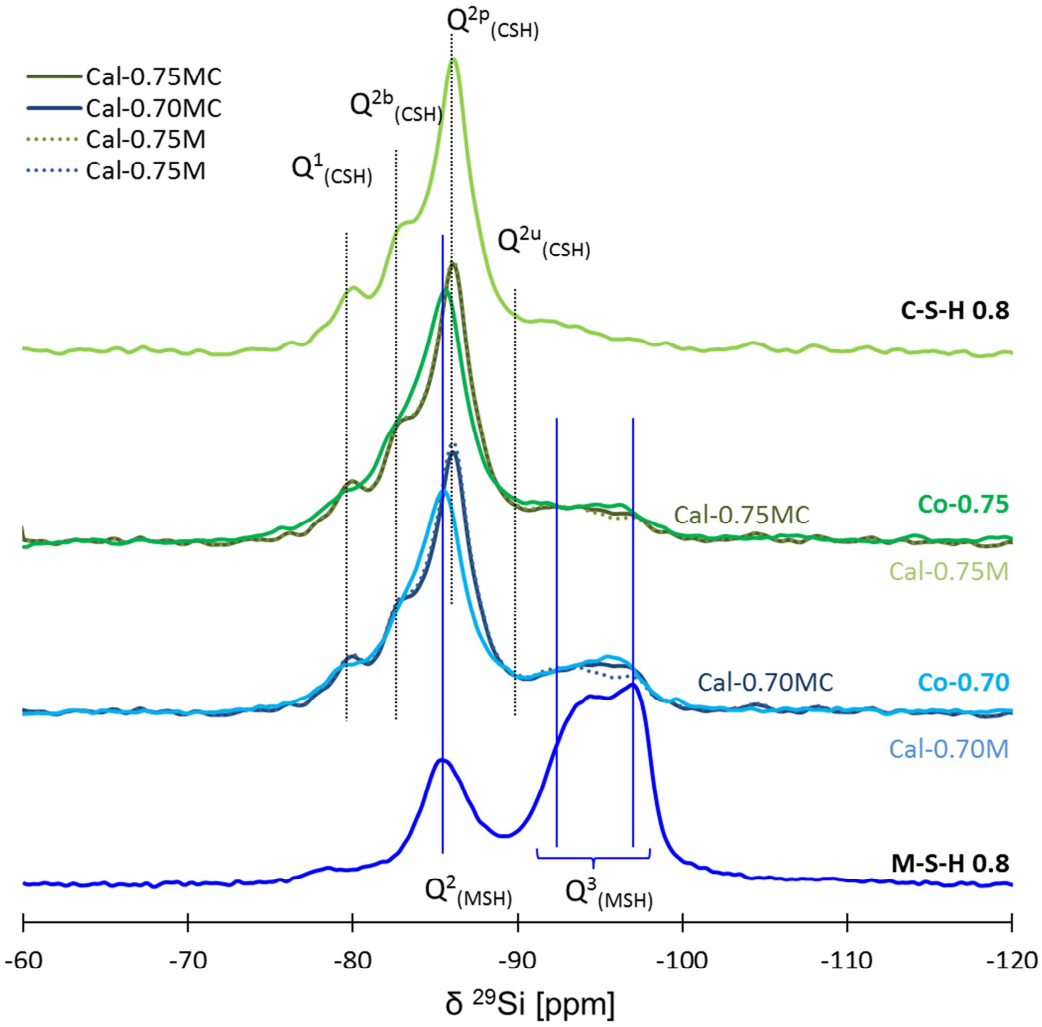

Figure 8: ^{29}Si MAS NMR spectra of Co-0.70 and Co-0.75 samples (1 year at 50°C) compared to spectra of C-S-H 0.8, M-S-H 0.8 and the calculated reference samples with M-S-H 0.8 (Cal-0.70M, Cal-0.75M) and with Co-0.05 (Cal-0.70MC, Cal-0.75MC).

Deconvolution of the ^{29}Si MAS NMR spectra was carried out following the procedure outlined in literature (Bernard et al., 2017a; Bernard et al., 2017b; L'Hôpital et al., 2016a; Nied et al., 2016) and the results are detailed in Table 3. Because of the formation of M-S-H, the content of silicate in C-S-H decreased from 96 (±5%) in pure C-S-H to 69 (±8%) in the Co-0.70 sample. The content of Q^1 and Q^2 sites attributed to C-S-H decreased with the replacement by magnesium. The calculated MCL remained above 20, which is typical for C-S-H with a low Ca/Si ratio.

The content of Q^3 tetrahedral sites between -92 and -97 ppm increased from 0 to 28% (±5%) (see Table 3) with the magnesium addition, confirming the presence of M-S-H. The amount of silicate attributed to M-S-H was higher than expected in Co-0.75 and Co-0.70 samples. The Mg/Si=0.8 in M-S-H and Ca/Si=0.8 in C-S-H should distribute the tetrahedral silicate to 6% in M-S-H and 94% in C-S-H and in 13% in M-S-H and 87% in C-S-H, respectively, for the two co-precipitated samples. ^{29}Si MAS NMR indicated the presence of significantly more tetrahedral silicate attributed to M-S-H (18% instead of 6% and 28% instead of 13%), indicating that the content of M-S-H is higher than expected (as detailed in Table 3).

The recorded ^{29}Si MAS NMR data were compared to calculated reference spectra (Cal-0.70MC and Cal-0.75MC) using a linear combination of the spectra of C-S-H 0.8 and Co-0.05 samples. This latter was preferred to pure M-S-H (Cal-0.70M and Cal-0.75M) since it provided a better fit of the experimental spectra, as shown in Figure 8.

This better agreement together with the high fraction of silicate attributed to pure M-S-H could be explained by some uptake of calcium in M-S-H also at higher pH. However, it remained unclear whether calcium was sorbed on the surface and edge sites of M-S-H only or whether it could be present in the octahedral layer as well.

Given the large amount of silicate associated with the M-(C)-S-H phase (28 and 18 % respectively, Table 3), all the magnesium in the solid fraction of the samples Co-0.70 and Co-0.75 seemed to be in M-(C)-S-H. This, together with the low magnesium concentration in solution, suggested no or very little incorporation of magnesium in C-S-H. The uptake of magnesium at the exchangeable sites of C-S-H could also be excluded as the CEC measurements showed the presence of mainly calcium (Table 4).

558 The TEM observations of Co-0.70 sample (**Error! Reference source not found.**) and the corresponding
559 EDS measurements (**Error! Reference source not found.**) showed two different types of products in
560 the sample. The first one contained mainly calcium and silicon and thus corresponded to C-S-H. The
561 second one, in smaller amount, contained significant amounts of magnesium and silicon, which
562 confirmed the presence of M-S-H. The M-S-H particles exhibited a layered texture which agreed well
563 with the sheet-like morphology already observed for pure M-S-H or mixed samples containing calcium
564 (Lothenbach et al., 2015; Roosz et al., 2015). The (Mg+Ca)/Si ratio remained lower than 0.8 regardless
565 the type of product. The mean Ca/Si and Mg/Si ratios were 0.65 ± 0.15 and 0.05 ± 0.05 respectively for
566 the C-S-H particles, and 0.15 ± 0.05 and 0.65 ± 0.15 for the M-S-H particles (**Error! Reference source**
567 **not found.**). This confirms the uptake of no or only very small amounts of magnesium in C-S-H, in
568 agreement with the ^{29}Si MAS NMR and PDF observations and indicates the possibility of a more
569 substantial uptake of calcium by M-S-H. However, as the EDS measurements were performed on areas
570 with a typical diameter of 100-150 nm, some intermixing of C-S-H and M-S-H phases can be expected,
571 such as for the data at Ca/Si ratios of 0.5 and 0.6 and Mg/Si ratios 0.3 to 0.6 which are based on
572 intermixing of C-S-H and M-S-H.

573
574 In summary, separate M-S-H (henceforward, M-(C)-S-H) and C-S-H phases were observed in the Co-
575 0.70 and Co-0.75 samples by TEM/EDS observations, ^{29}Si MAS NMR spectra, XRD and X-ray PDF
576 analysis. Traces of brucite were observed at 20°C after 2 years, due to the slow kinetic of brucite
577 dissolution in batch experiments (Bernard et al., 2017b; Szczerba et al., 2013). The data seemed to
578 indicate that a significant uptake of calcium in M-S-H occurred also at high pH. In C-S-H, however, no
579 or very limited uptake of magnesium seemed to occur. This result could be explained by the very low
580 magnesium concentrations in solution which resulted in a negligible fraction of charge balancing

581 magnesium at the C-S-H surface. The very low concentration of magnesium could also prevent its
582 incorporation in C-S-H during the precipitation process.

583 3.3. Effect on solubility

584 The solubility products of $C_{0.80}SH_{1.94}$ and $M_{0.78}SH_{1.48}$ were calculated using the measured concentrations
585 in solution at equilibrium (Figure 9 and Appendix A). The solubility product of $C_{0.80}SH_{1.94}$ remained
586 approximatively constant at ≃ -12 regardless of the presence or absence of magnesium. This indicates
587 that the uptake of magnesium by C-S-H and the formation of a solid-solution are rather unlikely. In
588 contrast, the decrease in the calculated solubility product of pure $M_{0.78}SH_{1.48}$ in the presence of calcium
589 by up to 1 log unit at the maximum showed a stabilization of M-S-H in the presence of calcium (Figure
590 9). This supported the formation of a solid-solution with an incorporation of calcium in M-S-H, in
591 agreement with the experimental observations.

592 The expected concentrations of calcium, magnesium and silicon were calculated using separate C-S-H
593 (Kulik, 2011) and M-S-H (Bernard et al., 2017b) phases, i.e. M-S-H without calcium and compared with
594 the measured data in Figure 1. The thermodynamic modelling pointed out that C-S-H was stable only at
595 pH higher than 10, in agreement with the experimental results. However, the calculated pH (10.4) in the
596 presence of magnesium (Co-0.05 and Co-0.10) was notably higher than the pH experimentally observed
597 (8.9 and 9.3 respectively) while the calculated silicon concentrations were lower than the experimental
598 ones (Appendix A). Such deviations between experiments and calculations may have resulted from the
599 occurrence of calcium in M-S-H which was neglected in this calculation. The uptake of calcium by M-
600 S-H would, indeed, reduce the pH values.

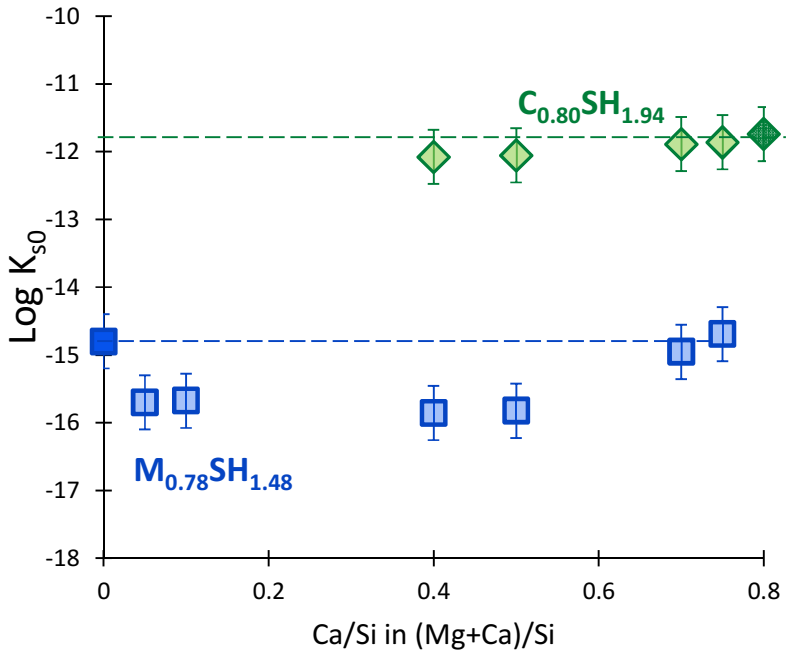

Figure 9: Solubility products of $M_{0.78}SH_{1.48}$ (squares) and solubility products of $C_{0.80}SH_{1.94}$ (diamonds) calculated for the co-precipitated samples at 20°C after 2 years. The M-S-H calculation is based on the end-members from Bernard et al. (Bernard et al., 2017b), the C-S-H calculation is derivated from (Kulik, 2011).

To check this assumption, two additional end-members with a Ca/Si ratio of 0.1 were introduced in the M-S-H solid solution model developed previously (Bernard et al., 2017b). The total of cation to silica ratios of 0.78 and 1.30 were kept constant, leading to the following stoichiometries: $M_{0.68}C_{0.1}SH_{1.48}$ and $M_{1.2}C_{0.1}SH_{1.80}$ as detailed in Table 2.

The calculated concentrations and atomic ratios in C-S-H and M-S-H (solid lines) are compared to the results obtained by the model containing only M-S-H and C-S-H (dashed lines) and with the experimental data (dots) in Figure 10. The experimentally observed calcium and silicon concentrations and pH measured experimentally were better described by the model taking into account the possible incorporation of calcium in M-S-H. The model was also able to predict the presence of calcium (Ca/Si up to 0.07) in M-S-H, in agreement with the experimental observations.

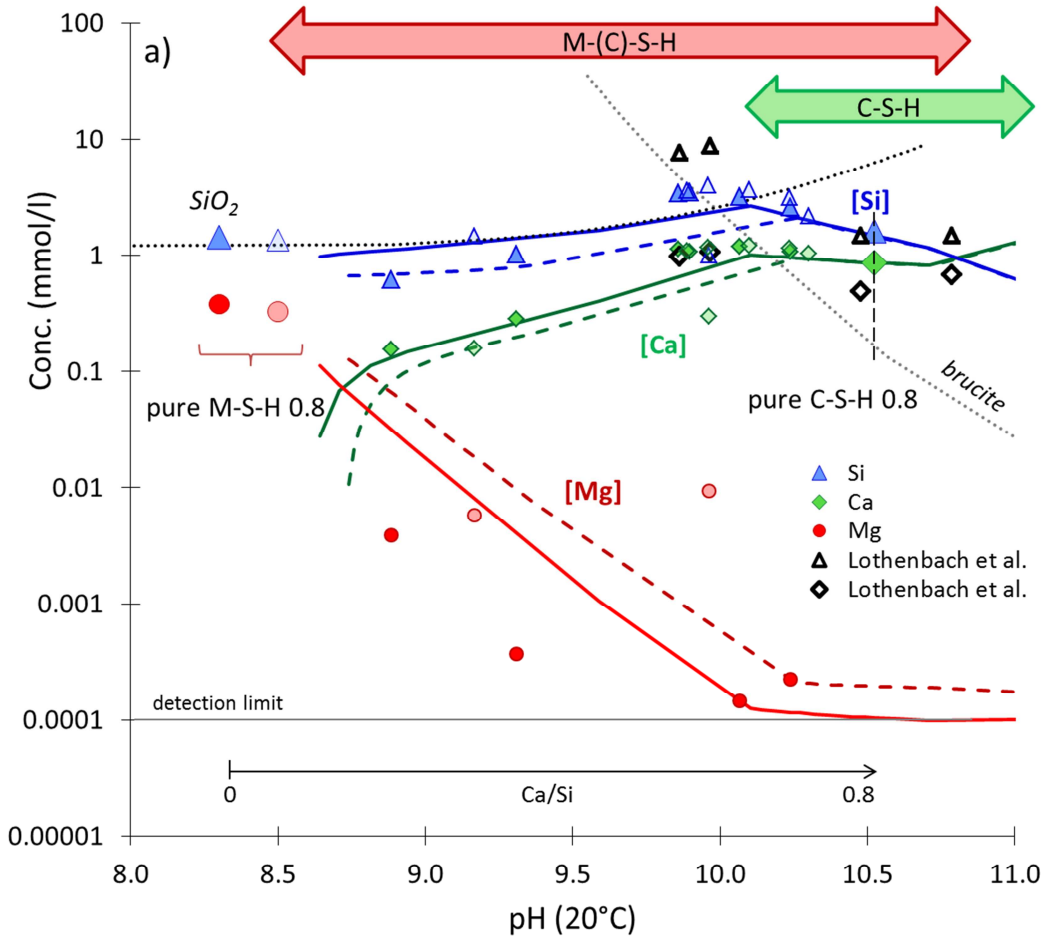

616

617

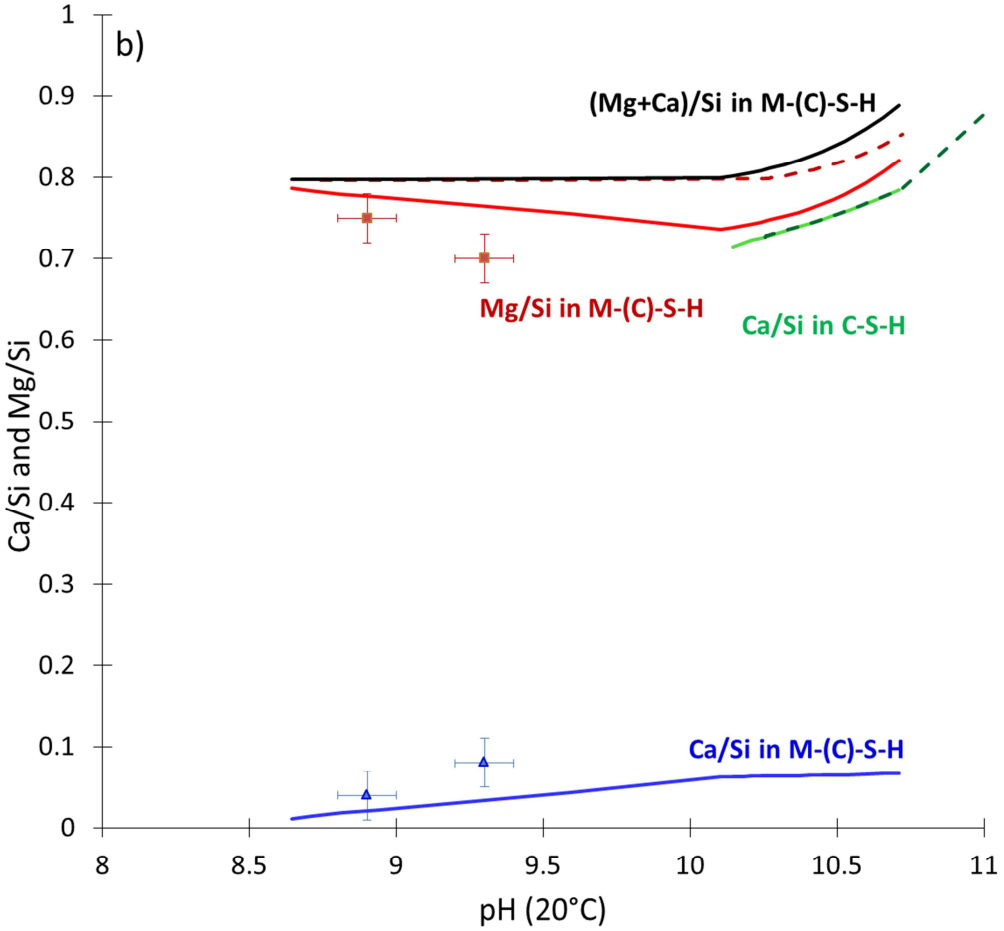

Figure 10: a) Calculated solubility curves (solid lines) associated to the co-precipitated samples using the M-(C)-S-H solution and C-S-H solid-solution models compared to the calculated solubility curves (dashed lines) using the M-S-H (Bernard et al., 2017b) and C-S-H solid-solution models. Solubilities of brucite and amorphous SiO_2 are shown in dotted lines. Empty symbols are from Lothenbach et al. (Lothenbach et al., 2015). b) Evolution of atomic ratios calculated by GEMS using the M-(C)-S-H solution and C-S-H solid-solution models compared to the M-S-H (Bernard et al., 2017b) and C-S-H solid-solution models and compared to the experimental results from mass balance.

4. Conclusions

This work aimed at investigating the relative stabilities of M-S-H and C-S-H and the possibility to incorporate small amounts of calcium into M-S-H, or small amounts of magnesium into C-S-H. The main conclusions can be summarized as follows.

1. C-S-H is unstable at pH values below 10.

2. When small amounts of calcium were added during the synthesis of M-S-H ((Mg+Ca)/Si = 0.8, Ca/Si = 0.05 or 0.10), the uptake of calcium by M-S-H is evidenced. CEC measurements showed that calcium is present as an exchangeable cation on the surface of M-S-H and is responsible for the less negative surface charge density of M-S-H particles measured by zeta potential. Nevertheless, a small fraction of the calcium incorporated into M-S-H may be non-exchangeable. Thermodynamic calculations confirm that an incorporation of calcium into M-S-H is likely since the presence of calcium stabilizes the M-S-H formed. A solid solution may thus occur between pure M-S-H and a M-C-S-H phase containing small amounts of calcium. The site of incorporation is not yet fully elucidated, nor the maximal uptake. However, the two additional end-members ($M_{0.68}C_{0.1}SH_{1.48}$ and $M_{1.2}C_{0.1}SH_{1.80}$) make it possible to describe the aqueous concentrations and solid compositions observed experimentally.

3. At pH values above 10, both M-S-H and C-S-H phases are stable and coexist. A similar uptake of calcium by M-S-H as at lower pH values is suggested. The simultaneous presence of C-S-H and M-S-H makes it difficult to evidence a possible uptake of magnesium by C-S-H. However, if such uptake occurs, it is not in the cation exchangeable sites and the incorporation of magnesium in the structure should be strongly limited by the very low concentration of magnesium in solution controlled by M-S-H.

The new solid solution model developed in this study to describe the uptake of calcium by M-S-H may offer new prospects to simulate the deterioration of calcium silicate cement-based materials in the presence of magnesium (provided by clayey minerals, ground- or seawater) or to optimize the design of novel binders containing calcium, magnesium and silicates.

Acknowledgements

The authors would like to thank Daniel Rentsch and Catherine Lerouge for helpful discussions, Remi Chassagnon for the TEM analyses, Numa Pfenninger for the ICP measurements, Luigi Brunetti and Fabien Le Goff for the support in the preparation of the samples and analysis. The NMR hardware was partially granted by the Swiss National Science Foundation (SNSF, grant no. 206021_150638/1).

References

Andersen, M.D., Jakobsen, H.J., Skibsted, J., 2003. Incorporation of aluminum in the calcium silicate hydrate (CSH) of hydrated Portland cements: a high-field ^{27}Al and ^{29}Si MAS NMR investigation. Inorganic Chemistry 42, 2280-2287.

Bach, T., Chabas, E., Pochard, I., Cau Dit Coumes, C., Haas, J., Frizon, F., Nonat, A., 2013. Retention of alkali ions by hydrated low-pH cements: Mechanism and Na^+/K^+ selectivity. Cement and Concrete Research 51, 14-21.

Bell, G., Bensted, J., Glasser, F., Lachowski, E., Roberts, D., Taylor, M., 1990. Study of calcium silicate hydrates by solid state high resolution ^{29}Si nuclear magnetic resonance. Advances in Cement Research 3, 23-27.

Bernard, E., Lothenbach, B., Le Goff, F., Pochard, I., Dauzères, A., 2017a. Effect of magnesium on calcium silicate hydrate (C-S-H). Cement and Concrete Research 97, 61-72.

Bernard, E., Lothenbach, B., Rentsch, D., Pochard, I., Dauzères, A., 2017b. Formation of magnesium silicate hydrates (M-S-H). Physics and Chemistry of the Earth, Parts A/B/C 99, 142-157.

Bonen, D., Cohen, M.D., 1992. Magnesium sulfate attack on portland cement paste—II. Chemical and mineralogical analyses. Cement and Concrete Research 22, 707-718.

Brew, D.R.M., Glasser, F.P., 2005. Synthesis and characterisation of magnesium silicate hydrate gels. Cement and Concrete Research 35, 85-98.

Chen, J.J., Thomas, J.J., Taylor, H.F., Jennings, H.M., 2004. Solubility and structure of calcium silicate hydrate. Cement and Concrete Research 34, 1499-1519.

Chiang, W.-S., Ferraro, G., Fratini, E., Ridi, F., Yeh, Y.-Q., Jeng, U., Chen, S.-H., Baglioni, P., 2014. Multiscale structure of calcium-and magnesium-silicate-hydrate gels. Journal of Materials Chemistry A 2, 12991-12998.

Conway, B., 1981. Ion hydration co-sphere interactions in the double-layer and ionic solutions. Journal of Electroanalytical Chemistry and Interfacial Electrochemistry 123, 81-94.

d'Espinose de Lacaillerie, J.-B., Kermarec, M., Clause, O., 1995. ^{29}Si NMR observation of an amorphous magnesium silicate formed during impregnation of silica with Mg(II) in aqueous solution. The Journal of Physical Chemistry 99(47), 17273-17281.

Dauzères, A., Achiedo, G., Nied, D., Bernard, E., Alahrache, S., Lothenbach, B., 2016. Magnesium perturbation in low-pH concretes placed in clayey environment - solid characterizations and modeling. Cement and Concrete Research 79, 137-150.

De Weerdt, K., Justnes, H., 2015. The effect of sea water on the phase assemblage of hydrated cement paste. Cement and Concrete Composites 55, 215-222.

Deschner, F., Winnefeld, F., Lothenbach, B., Seufert, S., Schwesig, P., Dittrich, S., Goetz-Neunhoeffer, F., Neubauer, J., 2012. Hydration of Portland cement with high replacement by siliceous fly ash. Cement and Concrete Research 42, 1389-1400.

Dove, P.M., Nix, C.J., 1997. The influence of the alkaline earth cations, magnesium, calcium, and barium on the dissolution kinetics of quartz. Geochimica et Cosmochimica Acta 61, 3329-3340.

Egami, T., Billinge, S.J.L., 2003. Chapter 3. The method of total scattering and atomic pair distribution function analysis. Pergamon Materials Series.

Garcia Calvo, J.L., Hidalgo, A., Alonso, C., Fernández Luco, L., 2010. Development of low-pH cementitious materials for HLRW repositories: Resistance against ground waters aggression. Cement and Concrete Research 40, 1290-1297.

Grangeon, S., Claret, F., Lerouge, C., Warmont, F., Sato, T., Anraku, S., Numako, C., Linard, Y., Lanson, B., 2013. On the nature of structural disorder in calcium silicate hydrates with a calcium/silicon ratio similar to tobermorite. Cement and Concrete Research 52, 31-37.

Gruner, J.W., 1934. The crystal structures of talc and pyrophyllite. Zeitschrift für Kristallographie-Crystalline Materials 88, 412-419.

Haas, J., Nonat, A., 2015. From C–S–H to C–A–S–H: Experimental study and thermodynamic modelling. Cement and Concrete Research 68, 124-138.

Jakobsen, U.H., De Weerdt, K., Geiker, M.R., 2016. Elemental zonation in marine concrete. Cement and Concrete Research 85, 12-27.

James, M., Hunter, R.J., O'Brien, R.W., 1992. Effect of particle size distribution and aggregation on electroacoustic measurements of. zeta. potential. Langmuir 8, 420-423.

Jenni, A., Mäder, U., Lerouge, C., Gaboreau, S., Schwyn, B., 2014. In situ interaction between different concretes and Opalinus clay. Physics and Chemistry of the Earth, Parts A/B/C 70, 71-83.

Jin, F., Al-Tabbaa, A., 2013. Thermogravimetric study on the hydration of reactive magnesia and silica mixture at room temperature. Thermochimica Acta 566, 162-168.

Klur, I., Pollet, B., Virlet, J., Nonat, A., 1998. CSH structure evolution with calcium content by multinuclear NMR, Nuclear magnetic resonance spectroscopy of cement-based materials. Springer, pp. 119-141.

Kulik, D., Wagner, T., Dmytrieva, S.V., Kosakowski, G., Hingerl, F., Chudnenko, K.V., Berner, U., 2013. GEM-Selektor geochemical modeling package: revised algorithm and GEMS3K numerical kernel for coupled simulation codes. Computational Geochemistry 17, 1-24.

Kulik, D.A., 2011. Improving the structural consistency of CSH solid solution thermodynamic models. Cement and Concrete Research 41, 477-495.

L'Hôpital, E., Lothenbach, B., Kulik, D., Scrivener, K., 2016a. Influence of calcium to silica ratio on aluminium uptake in calcium silicate hydrate. Cement and Concrete Research 85, 111-121.

L'Hôpital, E., Lothenbach, B., Scrivener, K., Kulik, D., 2016b. Alkali uptake in calcium alumina silicate hydrate (CASH). Cement and Concrete Research 85, 122-136.

L'Hôpital, E., Lothenbach, B., Le Saout, G., Kulik, D., Scrivener, K., 2015. Incorporation of aluminium in calcium-silicate-hydrates. Cement and Concrete Research 75, 91-103.

Labbez, C., Nonat, A., Pochard, I., Jönsson, B., 2007. Experimental and theoretical evidence of overcharging of calcium silicate hydrate. Journal of Colloid and Interface Science 309, 303-307.

Labbez, C., Pochard, I., Jönsson, B., Nonat, A., 2011. CSH/solution interface: Experimental and Monte Carlo studies. Cement and Concrete Research 41, 161-168.

Le Saout, G., Lécolier, E., Rivereau, A., Zanni, H., 2006. Chemical structure of cement aged at normal and elevated temperatures and pressures: Part I. Class G oilwell cement. Cement and Concrete Research 36, 71-78.

Leisinger, S.M., Bhatnagar, A., Lothenbach, B., Johnson, C.A., 2014. Solubility of chromate in a hydrated OPC. Applied Geochemistry 48, 132-140.

Lequeux, N., Morau, A., Philippot, S., Boch, P., 1999. Extended X-ray Absorption Fine Structure Investigation of Calcium Silicate Hydrates. Journal of the American Ceramic Society 82, 1299-1306.

Lerouge, C., Gaboreau, S., Grangeon, S., Claret, F., Warmont, F., Jenni, A., Cloet, V., Mäder, U., 2017. In situ interactions between Opalinus Clay and Low Alkali Concrete. Physics and Chemistry of the Earth, Parts A/B/C 99, 3-21.

Lothenbach, B., Durdzinski, P., DeWeerdt, K., 2016. Thermogravimetric analysis, in: Scrivener, K., Snellings, R., Lothenbach, B. (Eds.), A Practical Guide to Microstructural Analysis of Cementitious Materials. CRC Press, Oxford, UK, pp. 177-212.

Lothenbach, B., Nied, D., L'Hôpital, E., Achiedo, G., Dauzères, A., 2015. Magnesium and calcium silicate hydrates. Cement and Concrete Research 77, 60-68.

Lothenbach, B., Nonat, A., 2015. Calcium silicate hydrates: Solid and liquid phase composition. Cement and Concrete Research 78, 57-70.

MacKenzie, K., Meinhold, R., 1994. The thermal reactions of talc studied by 29 Si and 25 Mg MAS NMR. Thermochimica Acta 244, 195-203.

Mäder, U., Jenni, A., Lerouge, C., Gaboreau, S., Miyoshi, S., Kimura, Y., Cloet, V., Fukaya, M., Claret, F., Otake, T., Shibata, M., Lothenbach, B., 2017. 5-year chemico-physical evolution of concrete-claystone interfaces. Swiss Journal of Geosciences 110, 307-327.

Mägi, M., Lippmann, E., Samoson, A., Engelhardt, G., Grimmer, A.R., 1984. Solid-state high-resolution silicon-29 chemical shifts in silicates. The Journal of Physical Chemistry 88, 1518-1522.
Martin, L.H., Winnefeld, F., Tschopp, E., Müller, C.J., Lothenbach, B., 2017. Influence of fly ash on the hydration of calcium sulfoaluminate cement. Cement and Concrete Research 95, 152-163.
Massiot, D., Fayon, F., Capron, M., King, I., Le Calvé, S., Alonso, B., Durand, J.O., Bujoli, B., Gan, Z., Hoatson, G., 2002. Modelling one-and two-dimensional solid-state NMR spectra. Magnetic Resonance in Chemistry 40, 70-76.
Meral, C., Benmore, C., Monteiro, P.J., 2011. The study of disorder and nanocrystallinity in C–S–H, supplementary cementitious materials and geopolymers using pair distribution function analysis. Cement and Concrete Research 41, 696-710.
Myers, R.J., L'Hôpital, E., Provis, J.L., Lothenbach, B., 2015. Effect of temperature and aluminium on calcium (alumino)silicate hydrate chemistry under equilibrium conditions. . Cement and Concrete Research 68, 83-93.
Nied, D., Enemark-Rasmussen, K., L'Hopital, E., Skibsted, J., Lothenbach, B., 2016. Properties of magnesium silicate hydrates (MSH). Cement and Concrete Research 79, 323-332.
Pedone, A., Palazzetti, F., Barone, V., 2017. Models of Aged Magnesium–Silicate–Hydrate Cements Based on the Lizardite and Talc Crystals: A Periodic DFT-GIPAW Investigation. The Journal of Physical Chemistry C.
Peyronnard, O., Benzaazoua, M., Blanc, D., Moszkowicz, P., 2009. Study of mineralogy and leaching behavior of stabilized/solidified sludge using differential acid neutralization analysis: Part I: Experimental study. Cement and Concrete Research 39, 600-609.
Plusquellec, G., Nonat, A., 2016. Interactions between calcium silicate hydrate (CSH) and calcium chloride, bromide and nitrate. Cement and Concrete Research 90, 89-96.
Qiu, X., Thompson, J.W., Billinge, S.J., 2004. PDFgetX2: a GUI-driven program to obtain the pair distribution function from X-ray powder diffraction data. Journal of Applied Crystallography 37, 678-678.
Renaudin, G., Russias, J., Leroux, F., Cau-dit-Coumes, C., Frizon, F., 2009. Structural characterization of C–S–H and C–A–S–H samples—Part II: Local environment investigated by spectroscopic analyses. Journal of Solid State Chemistry 182, 3320-3329.
Richardson, I.G., 2008. The calcium silicate hydrates. Cement and Concrete Research 38, 137-158.

Richardson, I.G., Brough, A.R., Brydson, R., Groves, G.W., Dobson, C.M., 1993. Location of aluminum in substituted calcium silicate hydrate (C-S-H) gels as determined by ^{29}Si and ^{27}Al NMR and EELS. Journal of the American Ceramic Society 76, 2285-2288.

Richardson, I.G., Skibsted, J., Black, L., Kirkpatrick, R.J., 2010. Characterisation of cement hydrate phases by TEM, NMR and Raman spectroscopy. Advanced Cement Based Materials 22, 233-248.

Roosz, C., Grangeon, S., Blanc, P., Montouillout, V., Lothenbach, B., Henocq, P., Giffaut, E., Vieillard, P., Gaboreau, S., 2015. Crystal structure of magnesium silicate hydrates (MSH): The relation with 2: 1 Mg–Si phyllosilicates. Cement and Concrete Research 73, 228-237.

Santhanam, M., Cohen, M.D., Olek, J., 2002. Mechanism of sulfate attack: a fresh look: part 1: summary of experimental results. Cement and concrete research 32, 915-921.

Sato, H., Grutzeck, M., 1991. Effect of starting materials on the synthesis of tobermorite, MRS Proceedings, 245. Cambridge Univ Press, pp. 235-240.

Shi, C., Stegemann, J., 2000. Acid corrosion resistance of different cementing materials. Cement and Concrete Research 30, 803-808.

Skibsted, J., Henderson, E., Jakobsen, H.J., 1993. Characterization of calcium aluminate phases in cements by aluminum-^{27}MAS NMR spectroscopy. Inorganic chemistry 32, 1013-1027.

Skinner, L., Chae, S., Benmore, C., Wenk, H., Monteiro, P., 2010. Nanostructure of calcium silicate hydrates in cements. Physical review letters 104, 195502.

Swanton, S., Heath, T., Clacher, A., 2016. Leaching behaviour of low Ca: Si ratio CaO–SiO 2–H 2 O systems. Cement and Concrete Research 88, 82-95.

Szczerba, J., Prorok, R., Śnieżek, E., Madej, D., Maślona, K., 2013. Influence of time and temperature on ageing and phases synthesis in the $MgO–SiO_2–H_2O$ system. Thermochimica Acta 567, 57-64.

Thoenen, T., Hummel, W., Berner, U., Curti, E., 2014. The PSI/Nagra Chemical Thermodynamic Database 12/07. PSI report 14-04, Villigen PSI, Switzerland.

Viallis-Terrisse, H., Nonat, A., Petit, J.-C., 2001. Zeta-potential study of calcium silicate hydrates interacting with alkaline cations. Journal of colloid and interface science 244, 58-65.

Walling, S.A., Kinoshita, H., Bernal, S.A., Collier, N.C., Provis, J.L., 2015. Structure and properties of binder gels formed in the system $Mg(OH)_2$-SiO_2-H_2O for immobilisation of Magnox sludge. Dalton Transactions 44, 8126-8137.

White, C.E., 2016. Effects of temperature on the atomic structure of synthetic calcium–silicate–deuterate gels: A neutron pair distribution function investigation. Cement and Concrete Research 79, 93-100.

White, C.E., Daemen, L.L., Hartl, M., Page, K., 2015. Intrinsic differences in atomic ordering of calcium (alumino) silicate hydrates in conventional and alkali-activated cements. Cement and Concrete Research 67, 66-73.

White, C.E., Provis, J.L., Bloomer, B., Henson, N.J., Page, K., 2013. In situ X-ray pair distribution function analysis of geopolymer gel nanostructure formation kinetics. Physical Chemistry Chemical Physics 15, 8573-8582.

Zhang, T., Cheeseman, C., Vandeperre, L., 2011. Development of low pH cement systems forming magnesium silicate hydrate (MSH). Cement and Concrete Research 41, 439-442.

Highlights:

- C-S-H is unstable at pH values below 10
- At pH values between 10 and 10.5, M-S-H and C-S-H phases are stable and coexist
- A calcium uptake occurs in M-S-H, at the cation exchange sites, potentially at other sites
- A solid solution model can be used to describe the calcium uptake in M-S-H: M-(C)-S-H